2011

Pore-scale lattice Boltzmann simulations of inertial flows in realistic porous media: a first principle analysis of the Forchheimer relationship

Chukwudi Paul Chukwudozie
Louisiana State University and Agricultural and Mechanical College, chuckdii2002@yahoo.com

PORE-SCALE LATTICE BOLTZMANN SIMULATIONS OF INERTIAL FLOWS IN REALISTIC POROUS MEDIA: A FIRST PRINCIPLE ANALYSIS OF THE FORCHHEIMER RELATIONSHIP

A Thesis

Submitted to the Graduate Faculty of the
Louisiana State University and
Agricultural and Mechanical College
in partial fulfillment of the
requirements for the degree of

Master of Science in Petroleum Engineering

in

The Craft & Hawkins Department of Petroleum Engineering

by
Chukwudi Chukwudozie
B.Eng., Chemical Engineering, Federal University of Technology, Minna, 2006
May 2011

Acknowledgments

My sincere gratitude goes to the following; My advisor, Dr. Mayank Tyagi for the opportunity to work under him and for providing me with guidance and the resources that made this project a success; my committee members, Drs. Christopher White and Karsten Thompson for their invaluable contributions and criticisms that have given shape to this work; Drs. Stephen Sears, Clinton Willson and other members of the non-Darcy group. I am also grateful to ExxonMobil Production Company for the financial support of this project and my studies. I want to thank the Craft and Hawkins department, the Chair and Faculty of Petroleum Engineering for giving me the opportunity to undertake my graduate studies, for the invaluable knowledge gained during my studies and the discussions I benefitted from while carrying out this work. I express my gratitude to the poresim research consortium (www.poresim.org) of the department of Chemical Engineering, Louisiana State University (LSU), for graciously granting me access to the CT image file of the random sphere pack for used in this work and also to the OpenLB group (www.lbmethod.org) for the open source code which was used to implement the LBM algorithm

I am appreciative of my friends and colleagues with whom I shared and gained useful ideas. This includes, Nathan Lane, Ali Takbiri, Pradeep Bhattad, Yijie Shen, Mohammed Zulqarnain and Paulina Mwangi. In addition, I acknowledge the Louisiana Optical Network Initiative (LONI) and the Center for Computation and Technology (CCT) at LSU for granting me access to High Performance Computing (HPC) resources on which the simulations in this work were carried out. I also thank the members of staff at the CCT, especially Dr. Le Yan for helping me resolve some of the problems I faced while using the HPC systems.

Finally, I am eternally indebted to my parents and siblings for the love and moral support they have given to me throughout my academic sojourn. Indeed, to them is this work dedicated.

Table of Contents

List of Tables

List of Figures

Abstract

With recent advances in the capabilities of high performance computing (HPC) platforms and the relatively simple representation of complex geometries of porous media, lattice Boltzmann method (LBM) has gained popularity as a means of solving fluid flow and transport problems. In this work, LBM was used to obtain flow parameters of porous media, study the behavior of these parameters at varying flow conditions and quantify the effect of roughness on the parameters by relating the volume averaged flow simulation results to Darcy and Forchheimer equations respectively.

To validate the method, flow was simulated on regular and random sphere arrays in cubic domains, for which a number of analytical solutions are available. Permeability and non-Darcy coefficients obtained from the simulation compared well with Kozeny and Ergun estimates while deviation from the observed constant permeability and tortuosity values occurred around $Re \approx 1 - 10$. By defining roughness as hemispherical protrusions on the smooth spheres in the regular array, it was observed from flow streamlines obtained at different roughness heights that the average length of the flow paths increased with increasing roughness height. As such, the medium tortuosity and non-Darcy coefficient increased while the permeability decreased as height of the roughness increased.

Applying the method to a 3D computed tomography image of Castlegate sandstone, the calculated macroscopic permeability and beta factor components were in good agreement with reported experimental values. In addition, LBM beta factors were compared with a number of empirical models for non-Darcy coefficient estimation and were found to be of the same order of magnitude as most of the correlations, although estimates of the models showed wide variation in values. Resolution of the original sample was increased by infilling

with more voxels and simulation in the new domain showed better flow field resolution and higher simulated flow regimes compared to those of the original sample, without significant change in the flow parameters obtained. Using the Reynolds number based on the Forchheimer coefficient, the range of transition from Darcy to non-Darcy regime was within the values reported by Ruth and Ma (1993) and Zeng and Grigg (2006).

Chapter 1
Introduction

1.1 Motivation and Objective

Porous media provide important path ways for fluid flow in many geophysical and engineering systems including petroleum reservoirs, and have continued to attract research interest for better understanding of flow behaviors to aid in investment decision making. Among the important parameters necessary to quantify single phase flow in such systems is the medium permeability which models flow at low Reynolds number and is obtained as the constant of proportionality in the continuum linear relationship between the applied pressure gradient and volume averaged flow rate in Darcy law. To perform economic analysis of reservoir engineering investments, conventional simulators use the diffusivity equation derived with Darcy's law for reservoir fluid flow performance analysis using permeability and other rock-fluid property data obtained from the field and experiments. However, at sufficiently high flow conditions, numerous observations suggest that the contribution of fluid inertia to pressure drop becomes significant such that permeability is no more a constant but varies with the flow conditions. In addition, with the easy-to-recover oils long gone and with more emphasis on production enhancement techniques, flow deviations from Darcy's law are common in fractured reservoirs especially around the wellbore. These deviations are attributed to inertial effect which in petroleum reservoirs is responsible for low productivity in near well regions due to flow convergence leading to significant pressure drop for a given velocity. Flow deviation is also encountered in gas reservoirs in which the contribution of inertia and gas slippage leads to nonlinearity. For such systems, conventional (Darcy law based) reservoir simulators underpredict reservoir performance since the fundamental governing equations do not properly model flow behavior in the reservoir. This has consequences some of which are difficulty in matching production data in history matching in addition to wrong investment

decisions made from the simulator results. To avoid these, it is necessary to model inertial flows and to obtain correct values of parameters for input in reservoir simulators.

Holditch and Morse (1976) in their numerical experiments showed that non-Darcy flows could reduce the effective conductivity of fractures near the wellbore region by a factor of about 20. As such, the primary motivation for understanding the non Darcy effects is to appropriately model the flow regime based on fundamental fluid dynamics with applications to porous media flow. Further, physics based models can be used to predict the onset of inertial effects along with quantifiable contribution to the overall process. A number of equations like the Forchheimer equation, Brinkman equation, the cubic law have been proposed to model fluid behavior in the regions of this deviation. Amongst all the available models, the quadratic Forchheimer equation is widely accepted and it quantifies the deviation in terms of the beta factor or Forchheimer coefficient. However, quantification of these parameters numerically is made difficult by the complex pore structure and irregular geometry of the system. Obtaining estimates of this parameter for real systems is one of the most challenging tasks of porous media modeling and simulation. This comes with challenges as it is difficult to obtain easy and accurate flow simulation in realistic media without modification of the complex topology and flow path. In addition, these flow quantities have been obtained from experiments and from analytical and empirical expressions that relate the macroscopic properties to some attributes of the porous media. However, the analytical expressions are only approximations for ideal cases while the empirical expressions have utility only in media similar to scenarios for which they were obtained and thus, are inaccurate when applied to a wide range of other media. Also, experimental determination of these parameters can be time consuming and expensive. In addition, they do not capture the effect of pore geometry on the flow field distribution and thus also, on the value of these quantities. Numerical experiments are cheaper; however, methods like network modeling depend on the simplification of the complex pore geometry while the finite difference (FD), finite elements (FE), and finite

volume (FV) methods respectively involve discretization of the Navier-Stokes (NS) equations and are even more challenging in solving for the variables on the complex pore/solid boundaries that line the entire media.

With advances in micro-imaging technology and its application for generation of accurate 3D models of porous media and the massive increase in computing power, an opportunity for accurate flow simulation and flow parameter quantification has been presented. The lattice Boltzmann method (LBM) is well placed to take benefit from these advances since it recovers the Navier - Stokes equation from the discrete Boltzmann equation. Unlike the conventional computational fluid dynamics (CFD) methods that are based on the macroscopic continuum equations, the LBM uses a mesoscopic equation to determine macroscopic fluid dynamics. It has the advantage of being flexible in the specification of variables in complex boundaries in terms of simple particle bounce back and reflection. This flexibility has opened up the potential for its use in modeling and simulating flow in complex systems like porous rocks. Since its algorithm is based on nearest neighbors, it is well suited for parallel computing and has taken advantage of the progressive increase in computing powers over the years.

1.2 Thesis Outline

This thesis presents the research work leading up to flow parameter quantification from results of flow simulation in porous media using the LBM. Chapter **2** introduces the concept of porous media flow outlining the different flow regimes, the regions and scenarios in a reservoir where they are encountered and the applicable equations for modeling flow in the Darcy and non-Darcy regimes respectively. A brief introduction to numerical methods for pore scale flow simulation is given while methods for reconstructing the pore scale geometry of porous media are mention and discussed.

In Chapter **3**, theory of the LB method is reviewed including the two common models,

viz. the Bhatnagar-Gross-Krook (BGK) and Multiple Relaxation time (MRT) models, and approaches for implementing the pressure gradient are mentioned. In addition, the source of errors likely to affect the LBM simulation results are reported while the conversion from LBM units to physical units are given.

Chapter **4** introduces the approach for using the kinetic models and the implementations of the driving force to simulate flow. Initial and boundary conditions applied are discussed while the method used for obtaining the flow parameters from the LBM simulation results is given. Also, the description of the geometries of the system whose flow parameters are obtained is presented.

Results of the flow simulations on the geometries described in Chapter **4** are presented in Chapter **5**, showing trends of the LBM calculated flow parameters at different Reynolds number and at different roughness levels. The flow parameters are also analyzed to quantify the onset of the deviation from Darcy's law using an appropriate dimensionless number.

Chapter **6** gives a summary of results of the present work and proposes directions for future work using the LBM.

Chapter 2
Fundamentals of Fluid Flow in Porous Media

Fluid flow problems are generally described by the Navier-Stokes (NS) equation derived from conservation of fluid mass and momentum. Due to the difficulty in solving the NS equations, approximate solutions are obtained by considering only the dominant forces acting within the fluids at particular flow conditions for different flow problems. In porous media, single phase flow is driven by two forces, viz; viscous force acting between the layers of fluids and the inertial force between fluids and the solid phases. As shown in Fig. 2.1, viscous forces dominate in the low pressure gradient regime with a corresponding linear relationship between the pressure gradient and volume averaged velocity. The solution of the NS equations in this viscous dominated region by neglecting the inertial forces produces Stokes equation, from which Darcy's law is obtained by volume averaging. Thus the linear/low pressure gradient regime is also known as Darcy regime in porous media studies.

With pressure gradient increase, the inertial forces between the fluid and the rock surfaces dominate with a non-linear pressure gradient with velocity. Stokes law and in effect, Darcy's law fail in this regime since they do not account for the increased influence of inertial effects at the higher pressures. Thus, it is necessary to properly understand this flow regimes and the regions in a reservoir where they occur for application of the proper equation.

In the following sections, the flow regimes and applicable governing equations will be analyzed in details with appropriate parameters that quantify flow in those regimes.

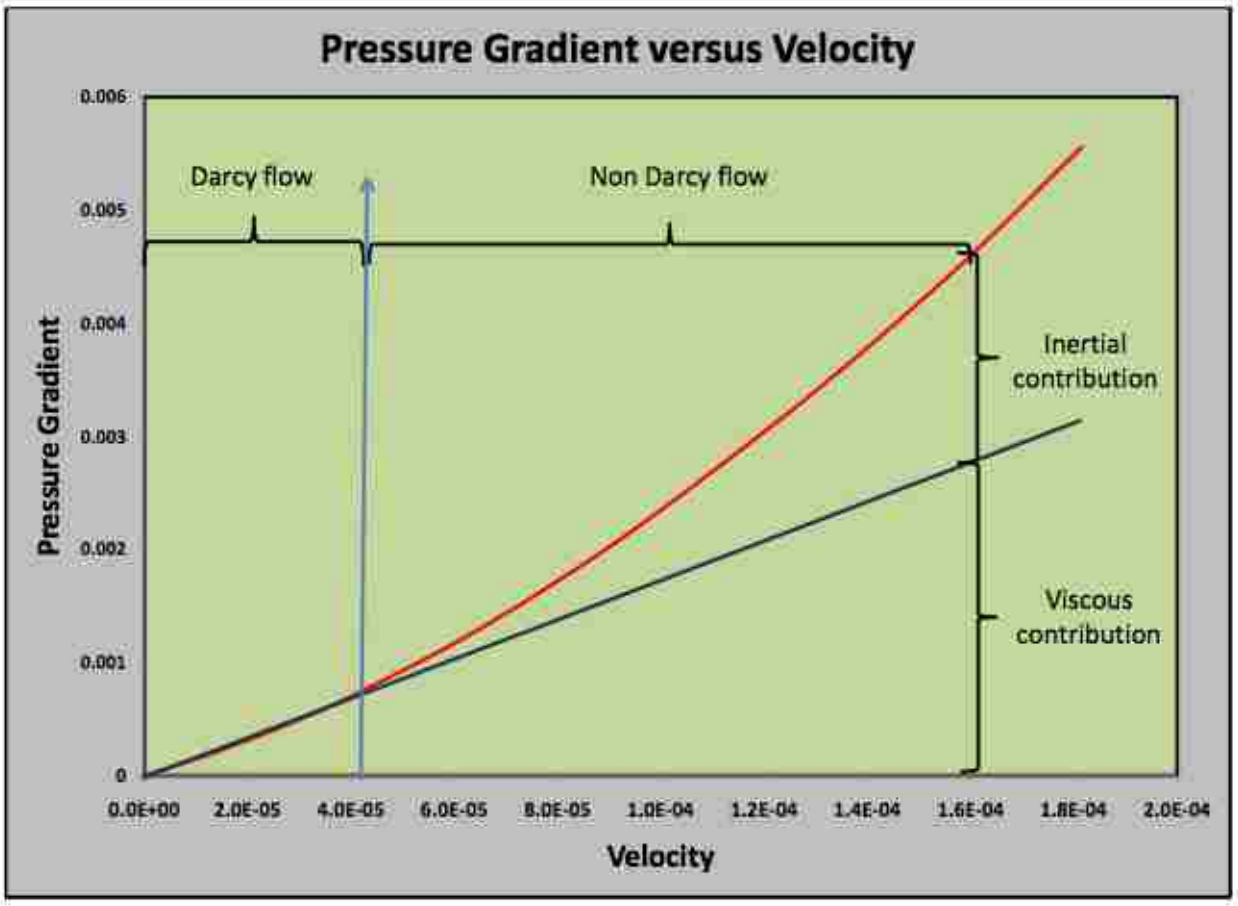

Figure 2.1: Typical flow regimes in porous media.

2.1 Darcy Flows

Darcy flow is common in the bulk of the reservoir, far away from the well where the dominant viscous force produces a creeping motion of the reservoir fluid. In this regime, the Reynolds number (Re), given in Equation 2.1, is small (O[1]) and the flow is dominated by fluid viscous forces, such that the pressure gradient responsible for the flow is linearly proportional to the superficial velocity.

$$Re = \frac{\rho u D_p}{\mu} \tag{2.1}$$

Darcys law which is the common equation used in petroleum reservoir engineering to model fluid flow in this regime is given by

$$\vec{u} = \frac{K}{\mu}\nabla p \tag{2.2}$$

K, the permeability tensor is a medium property that acts on the pressure gradient and transforms it into the velocity vector.

2.1.1 Permeability

The medium permeability is obtained from numerous experiments in which a fluid is made to flow through a sample of a porous medium for a given applied pressure gradient, and the volumetric flow rate measured from which the permeability is obtained as in Equation 2.2. Permeability is highly dependent on the size, distribution and connectivity of the pore spaces and it defines the physical relationship between the porous media, the fluid that flows through it and the conditions imposed by the flow process. Thus, a quantitative and qualitative prediction of this property in porous media requires an accurate microscopic model of the porous media and an understanding of the contribution of the microstructure of the medium to flow distribution. The continuum scale experimental methods neither capture the effect of tortuosity, pore space irregularity and other microscopic details of the rock on the permeability, nor deliver the flow distribution in the pores. Since the full permeability tensor of reservoir rocks is difficult to measure, empirical relations are often used to estimate permeability through pore structure parameters. The simplest micro-scale approach to predict the permeability taking into account the pore geometry is the one provided by Kozeny and Carman, given below, derived from the Hagen-Poiseuille equation for flow in a pipe.

$$q = uA = -\frac{\pi R^4}{8\mu}\frac{\Delta p}{L} \tag{2.3}$$

q: Volumetric flow rate; A: cross sectional area. On comparison with the Darcy law and eliminating the length with the tortuosity and replacing the radius with the hydraulic radius, the intrinsic permeability becomes

$$k = \frac{D_p^2}{8\tau(1-\phi)^2 a_v^2} \tag{2.4}$$

τ = tortuosity, a_v = specific surface area (surface area/rock volume) and D_p =particle diameter. These properties are combined into a geometric factor, A_p.

$$k = \frac{\phi^3 D_p^2}{A_p(1-\phi)^2} \qquad A_p = 8\tau a_v^2 = 72\tau \tag{2.5}$$

$A_p = 150$ and 180 for Kozeny-Carman and Ergun equations respectively . Other empirical relations exist in the literature for estimating permeability from microscopic geometric quantities and are widely used because they are easy and simple to understand. However, these relations introduce geometric quantities like the permeability, specific surface area, formation factor, etc that are not readily measured from experiments, especially for complicated systems.

2.1.2 Tortuosity (τ)

Fluid flow through porous media is influenced by the microscopic properties of the media like volume and structure of the pore spaces. The amount of void spaces is quantified by the medium porosity while the complex pathways of these spaces are quantified using a property known as the tortuosity. Tortuosity is a tensor and its components are defined as the square of the ratio of the actual distance traveled by the fluid to the length of the media in the direction of the pressure gradient. The concept was introduced by Carman as a

corrective factor needed to model the influence of the tortuousness of the domain available for displacement of a fluid phase.

$$\tau = \left(\frac{L_e}{L}\right)^2 \tag{2.6}$$

L and L_e are the length of the media and the actual distance traveled by the fluid particles in the porous media. The definition of tortuosity stems from the fact that the pore spaces are connected into a network of complex and sinuous pathways so that the actual distance traveled by the particles is greater than the length of the media. According to Equation 2.6, a medium with straight paths parallel to the flow direction have tortuosities of one while the tortuosity of a medium with complicated pore space networks is greater than one. This property invariably affects the flow properties since reservoir rocks with tortuosity greater than one offer greater resistance to fluid flow and hence, have smaller permeabilities and larger beta factorsccompared to those whose tortuosity values are close to unity. Thus, although tortuosity is not explicitly captured in Darcy and Forchheimer equations respectively, it reflects in the values of permeability and beta factor. There are no established methods for measuring tortuosity. However, it has been estimated by geometrical analysis as in the bundle of tube method, experimentally using the NMR (Nuclear Magnetic Resonance) (Rigby and Gladden 1996) and numerically from flow simulation results (Nabovati and Sousa 2007). Using the result of these methods, empirical relations for tortuosity as a function of porosity and permeability have been developed.

2.2 Non-Darcy Flows

In regions close to the wellbore, it is observed that the pressure drop predicted by Darcys equation is lower than the actual values, indicating that some other effects, notably inertia, are responsible for the additional pressure drop. The behaviour is caused by the non-Darcy

effect, also known as the inertial effect. The contributions of these effects to flow are not captured by Darcy's law since they have no significant impact at low Reynolds number. Investigators in gas flow technology frequently used the term turbulent and non-Darcy to describe viscous-inertial flow at high velocities near the wellbore of a gas well. The contribution of turbulence to the deviation from Darcy law has been ruled out since transition to the non-linear laminar flow regimes in porous media is gradual unlike the sharp change experienced in turbulence flows in pipe. In addition, the range of Reynolds number within which flow transition is observed is significantly higher in pipe flows than in flow through porous media.

Rushing et al. (2004) underlined that gas slippage and inertial flow may cause significant flow measurement errors. They attributed this to the result of convective flow as fluid particles move through tortuous rock pore throats of varying sizes. In the non-Darcy regime, the inertial contributions are marked by an increase in the pressure change without a proportionate increase in fluid velocity. This additional pressure change, they noted, is associated with the dissipation of inertial energy as fluid particles accelerate through smaller pore throats and decelerate thorough larger pore throats. Furthermore, the fluid acceleration creates secondary flow patterns and irreversible conversion of kinetic energy into heat through viscous shear. Ruth and Ma (1993) suggested that the fundamental reason for the nonlinear flow can be attributed to the microscopic inertial effect which alters the velocity and pressure fields. Hassanizadeh and Gray (1987) presented an order of magnitude analysis for the volume averaged equation and concluded that the microscopic viscous force is the source of the nonlinearity. The link between inertial effect and viscous dissipation was regarded as a paradox by Hassanizadeh and Gray (1987). This, they resolved when they considered that the pore scale convective inertial effect contributing to the form drag led to an increase in the total viscous dissipation. It is well known that if a fluid is inviscid, then boundary layer separation cannot occur if it flows through a porous media, therefore no form drag. The total drag around

the rock matrix consists of a linear dependent viscous drag as in Darcy flow and the form drag which is proportional to the square of velocity as obtained in the Forchheimer equation.

Despite the diverse opinions on the origin of the nonlinearity, it is generally accepted that the source of the deviation in the non-Darcy flow regime is microscopic inertial effect. This emphasizes the need to quantify the flow parameters from flow modeling and simulation carried out at the scale of the pore spaces.

2.2.1 Forchheimer Equation

Under high flow rate conditions, especially in regions around the wellbore and in gas reservoirs, the inertial forces may become large so that the linear relationship does not hold. Several criteria have been proposed to identify the threshold beyond which the linear relationship fails. The Reynolds number based on particle diameter is widely used and critical values between **1** and **10** obtained from experiments and numerical simulations have been reported in literature. In this regime, additional information is necessary to properly model flow since Darcy's law is insufficient to capture the non-linear behavior. In addition to several attempts, Forchheimer (1914) extended Darcy's law by adding a quadratic velocity term which is analogous to the inertia dependence on velocity squared in turbulent flows in fluid mechanics .

$$\frac{\Delta p}{L} = \frac{\langle u \rangle \mu}{k} + \beta \rho \langle u \rangle |\langle u \rangle| \tag{2.7}$$

β, is a medium property known as the beta factor (non-Darcy coefficient) which quantifies the amount of inertial contribution to the total pressure drop. Forchheimer equation, like Darcy's equation, originated empirically from experiments. Nevertheless, both equations have been derived from the NS equations using volume averaging and homogenization principles respectively (Ruth and Ma 1993), (Ruth and Ma 1992), (Whitaker 1999) and (Whitaker

1996). At low Reynolds number flows characteristic of laminar regimes, the contribution of inertia is insignificant as the square of the velocity is negligible. Thus, the Forchheimer equation reduces to Darcy's law in viscous dominated laminar flows. Even the Forchheimer equation has been subject of numerous criticisms as Ruth and Ma (1993), Barree and Conway (2004) and Huang and Ayoub (2006) doubted the ability of the quadratic velocity term to capture all regions beyond the Darcy flow. However, the objective of this work is not to put the numerous empirical relations to further test, but to calculate the permeability and beta factor for Darcy's and Forchheimer's equations respectively, from LBM simulation results

2.2.2 Forchheimer Coefficient/Beta Factor (β)

The Forchheimer coefficient quantifies the extent of flow deviation from the linear Darcy's regime. In the non-Darcy regime, dissipation increases due to inertial contribution to flow and this affects the apparent medium permeability. In this region, the permeability is not constant but varies with flow velocity and is used with the beta factor to model flow. Generally, in the petroleum industry, the beta factor is assumed to be a constant and is normally obtained as the slope of the inverse of the apparent permeability obtained in the non-Darcy regime versus a pseudo Reynolds $\left(\frac{\rho u}{d}\right)$ number.

$$\frac{1}{k_{app}} = \frac{1}{\mu\langle u\rangle}\frac{\Delta p}{L} = \frac{1}{k_{int}} + \frac{\beta\rho|\langle u\rangle|}{\mu} \tag{2.8}$$

Like the permeability, β is a tensor. It is constant in the range of the Forchheimer regime and is a property of the porous medium like permeability, tortuosity, porosity etc. A number of empirical and analytical expressions have been proposed to estimate the beta factor with the simplest being the Ergun equation modeled for collection of spheres and for cylindrical conduits using the bundle of tube model and from which the permeability can also be obtained. According to Ergun (1952), the non-Darcy coefficient and permeability are proportional to the particle/conduit diameter and medium porosity as given below.

$$\nabla p = \frac{150\mu(1-\phi)^2\langle\vec{u}\rangle}{\phi^3 D_p^2} + \frac{1.75(1-\phi)\rho\langle\vec{u}\rangle^2}{\phi^3 D_p} \tag{2.9}$$

$$\beta = \frac{1.75(1-\phi)}{\phi^3 D_p} \tag{2.10}$$

$$k = \frac{\phi^3 D_p^2}{150(1-\phi)^2} \tag{2.11}$$

Combining Equations 2.10 and 2.11, the Ergun beta factor related to the medium permeability and porosity is

$$\beta = \frac{0.142887}{k^{0.5}\phi^{1.5}} \tag{2.12}$$

In addition to the Ergun equation, a large number of empirical relations based on experimental data have been developed, viz., Thauvin and Mohanty (1998), Geerstma (1974), Coles and Hartman (1998) correlations to mention a few. Hernandez (2004) reported that most of these correlations for beta factor have an inverse relationship with permeability and porosity and can all be summarized into a form similar to Equation 2.12.

$$\beta = \frac{a}{k_f^b \phi_p^c} \tag{2.13}$$

k_f is medium permeability, **a** and **c** are constants whose values differentiate the correlations while **b** must be 0.5 for the unit of beta factor to be inverse of length. The wide range of correlations available in literature for predicting permeability and beta factor underscores the importance of these flow parameters and how easy it is desired for them to be obtained for input in reservoir simulators. For complex media however, the Ergun equation and other

empirical correlations may not accurately predict the beta factor since they have been developed to be applicable to particular media. Thus, the Forchheimer coefficient obtained for a given medium differ for different correlations. This was confirmed by Jones (1987) in which he showed a two order of magnitude difference in the inertial coefficient obtained from different correlations for a given medium permeability. However, there is need to accurately quantify the value of these parameters and to estimate the impact of the beta factor on flow deviations from Darcy' s law. Ruth and Ma (1993) in their paper suggested that if the Forchheimer effects are to be properly studied, very detailed knowledge of the microscopic flow field must be obtained. Continuing, they noted that it is insufficient to simply know the structure of the porous media-the flow patterns in the various flow regimes must also be known.

The empirical relations treat porous media as continuum. As a result, flow distribution in the individual pore and solid phases are not identified. Numerical methods on the other hand, solves the flow equations in the individual pore spaces and on the boundary between the two phases to produce the flow distribution for the whole domain which is averaged and arranged in the form of the empirical relations to obtain the flow parameters.

2.3 Overview of Numerical Approaches

Numerical simulations of fluid flow in 3D pore structure can, in principle, provide accurate estimations of permeability and beta factor if an accurate model of the real medium is available. The 3D model is often created by the computed tomography imaging or from statistically reconstructed samples from 2D thin sections. The pore boundaries of real porous media are arbitrarily complex and this poses a major challenge in specifying boundary values of the variables and solving the flow problem using the conventional FD, FV and FE methods to discretize the Stokes equation. The LBM solves this problem and has established itself as a credible alternative to the conventional Navier-Stokes solvers. It is a relatively new

method and has been used extensively by Feichtinger (2005), Guo and Zheng (2002), Chen, Martinez, and Mei (1996), He et al. (1997), and Mei et al. (2000) to simulate incompressible Couette, lid driven and Poisueille flows respectively and produced good results that compare well with analytical formulas. Unlike the conventional computational fluid dynamics (CFD) methods based on the macroscopic continuum equations, the LBM uses a mesoscopic equation, specifically the Boltzmann equation to determine macroscopic fluid dynamics. It has the advantage of being flexible in the specification of variables on complex boundaries in terms of simple particle bounce back and reflection. This flexibility has opened up the potential in its use for modeling and simulating flow in complex media like porous rocks. Since its algorithm is based on nearest neighbors, it is adaptive to parallel computing and has taken advantage of the progressive increase in computing powers over the years.

The earliest known applications of the LBM in porous media simulation are by Succi, Foti, and Higuera (1989) and Cancelliere et al. (1990). They used the method to estimate the permeability of 3-D porous media and obtained values that were comparable to the Kozeny equation. Thereafter, Rothman (1988) and Ferreol and Rothman (1995) used the method to simulate single phase and 2-phase flow in the Fountainbleau sandstone. Recently, Jin, Patzek, and Silin (2004) built virtual samples of consolidated and unconsolidated reservoir rocks by applying the physics based reconstruction approach and directly calculated the absolute permeability of the medium using results obtained from the LBM simulation of flow in the domain. Torskaya, Jin, and Verdin (2007) studied the relationship between permeability and irreducible water saturation, represented by the amount of clay deposited on the solid phase of the porous medium. Using the LBM on a synthetic generated 3D image of the pore space domain the permeability was estimated for different morphology of dispersed clay in the medium. The results of these numerous efforts compared well with appropriate analytical and experimental data. However, most of the earlier efforts either used the single relaxation time BGK model which is highly dependent on simulation parameters or treated

the permeability and the beta factor as a single scalar quantity without any estimate of the tortuosity.

2.4 Pore-Scale Representation of Porous Media

2.4.1 Reconstruction of Microstucture of Porous Media

Flow simulation for rock property prediction is not possible without an accurate reconstruction of the porous media geometry. Thus, it is absolutely necessary to have a 3D model of the pore space. Jin, Patzek, and Silin (2004) reported that the following three approaches are commonly used to reconstruct the microstructures of natural rocks.

1. **Experimental Approach:** This approach includes serial sectioning, which is based on the combination of a series of 2D sections to form a 3D image (Lin and Cohen 1982) and X ray computed tomography which uses non destructive X-ray computed tomography to image the 3D pore space of realistic porous media at resolution of the order of microns. These methods are time consuming, expensive and unrealistic especially when they are required to account for pore spaces in the sub micron regime, that are common abundant in carbonates (Okabe 2004).

2. **Statistical Approach:** This includes the two-point correlation function measured from 2D thin section of real rocks. The correlation function is used with other geometric properties such as porosity to generate a 3D image with the same statistical properties as the original 2D thin section. A relatively new method is the multiple point statistics to generate 3D images based on two dimensional thin sections (Okabe 2004). These methods however, fail to reproduce the long range connectivity of the pore space (Oren and Bakke 2003).

3. **The Process or Physics Based Reconstruction:** This approach generates the 3D microstructure by modeling the dynamic geological processes of sedimentation, compaction and diagenesis by which natural rocks are formed.

Okabe (2004) compared the 3D microstructures of Fointainebleau sandstone generated by the three different methods and reported that the process based method better reproduces the shapes of grains and pores of typical porous media.

2.4.2 Micro-Computed Tomography (CT) Imaging

Micro-CT imaging is a technique used to visualize and measure the geometric properties of interior of a porous media without sample preparation or chemical fixation. Typically, the spatial resolution is of the order of microns and must be smaller than the sizes of the void spaces for the pores to be captured in the digital scans.

A CT image is created by directing X-rays through the slice plane of the sample from multiple orientations and measuring their resultant decrease in intensity, to obtain an X-ray shadow image. These X-rays are scattered and/or absorbed as they pass through the sample. Attenuation of the x rays is primarily a function of X-ray energy and density and atomic number of the material being imaged. As a result, the mineral grains can be discriminated from the pore space in the images of the sample. A specialized algorithm is then used to reconstruct the distribution of X-ray attenuation in the slice plane of the shadow image into a gray scale image. By acquiring a stacked, contiguous series of CT images, data describing an entire volume is obtained. The gray scale image is thereafter thresholded to segment the data into pore and solid phases such that certain geometric properties like porosity of the original imaged sample are preserved.

2.4.3 Description of Segmented Porous Media

Porous media consists of two phases; Pore phase (P), Rock phase (M). The 3D image of the porous media obtained from CT scans is discretized and converted into a binary image so that the position vector $\vec{x}$ of the phases is described by:

[*] All real porous media used for simulations in this work were generated by CT imaging

$$I(\vec{x}) = \left(\begin{array}{lll} 0 & \text{for} & \vec{x} \in P \\ & & \\ 1 & \text{for} & \vec{x} \in M \end{array} \right); \qquad \vec{x} = x_i, x_j, x_k = 0, 1, \ldots N_i{-}1; 0, 1, \ldots N_j{-}1, 0, 1, \ldots N_k{-}1 \tag{2.14}$$

Chapter 3
Overview of Lattice Boltzmann Method (LBM)

The lattice Boltzmann method (LBM) is a numerical scheme for simulating fluid flow problems in terms of a single variable, the particle distribution function, compared to the traditional CFD methods that solve the N-S equation for the macroscopic variables such as pressure and velocity. The numerical scheme is derived from microscopic physics as it models fluids as a collection of parcels with some distribution of positions and momenta. The upscaled or coarse-grained dynamics of these parcels results in the macroscopic dynamics of the fluid. Although the method is derived from microscopic physics, it is able to recover accurately, solutions of the N-S equations in the hydrodynamic limit of low Mach number (Succi, Foti, and Higuera 1989). The desired macroscopic variables can be recovered as moments of the distribution function. It finds favor in pore scale modeling because of the flexibility with which it treats complex boundary conditions in terms of particle reflection and bounces at appropriate spatial locations flagged as wall sites.

3.1 Theory of LBM

The lattice Boltzmann equation is a discrete form of the continuous Boltzmann equation

$$\frac{\partial f_\alpha}{\partial t} + e_\alpha f_\alpha = \Omega \tag{3.1}$$

$f_\alpha(\vec{x}, \vec{e}_\alpha \partial t)$ is the fraction of fluid particles that have traveled in any of the phase space directions represented by α and Ω is the collision operator which will be described later. Evolution of the distribution is achieved by discretizing and solving a microscopic kinetic equation for the particle distribution function, $f_\alpha(\vec{x}, \vec{e}_\alpha \partial t)$, in each time step. In the method,

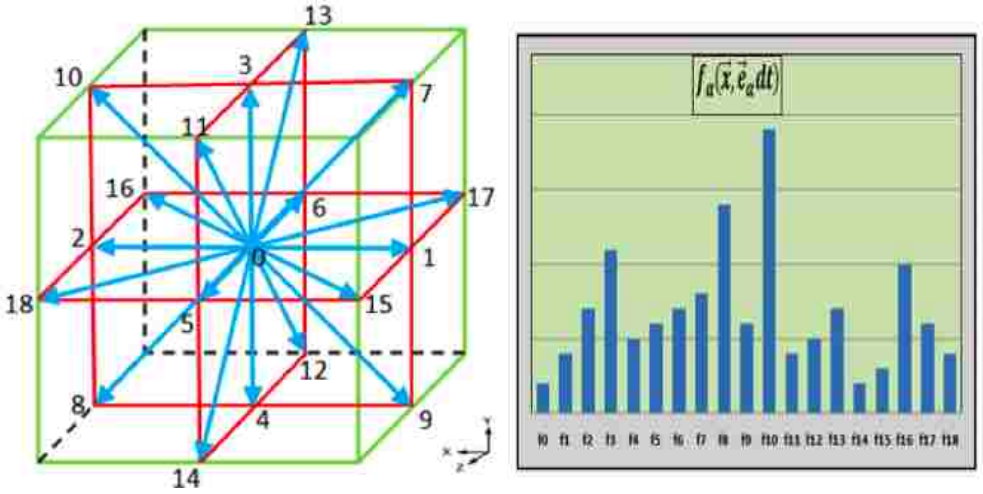

(a) D3Q19 Model.

(b) Bar plot of particle distribution for D3Q19 Model.

Figure 3.1: Velocity directions and distribution functions of particle on a typical 3D lattice node.

time and space are discretized with velocity limited to a finite set of vectors that represent the admissible directions in which the particles can travel. Different models with different particle directions are in use in the LBM for discretizing the three dimensional cubic lattice. For this work, the D3Q19 model will be used. The model is shown in Fig. 3.1. It has = 18 discrete cubic lattice velocities with a fluid particle at rest. Of the 18 directions, 6 are to the face centers while 12 are towards the edge centers of the cubic lattice as described in Equation 3.2.

$$e_\alpha = \begin{cases} (0,0,0); & \alpha = 0 \\ (\pm 1,0,0),(0,\pm 1,\pm 0),(0,0,\pm 1); & \alpha = 1,2,3,4,5,6 \\ (\pm 1,\pm 1,0),(\pm 1,0,\pm 1),(0,\pm 1,\pm 1); & \alpha = 7,8,9,10,11,12,13,14,15,16,17,18 \end{cases} \tag{3.2}$$

$\vec{e}_\alpha$: Vector of velocity direction

Other models like the D3Q15 and D3Q27 are available. The D3Q15 model requires less computation per iteration, however, it provides less accurate results and has been reported

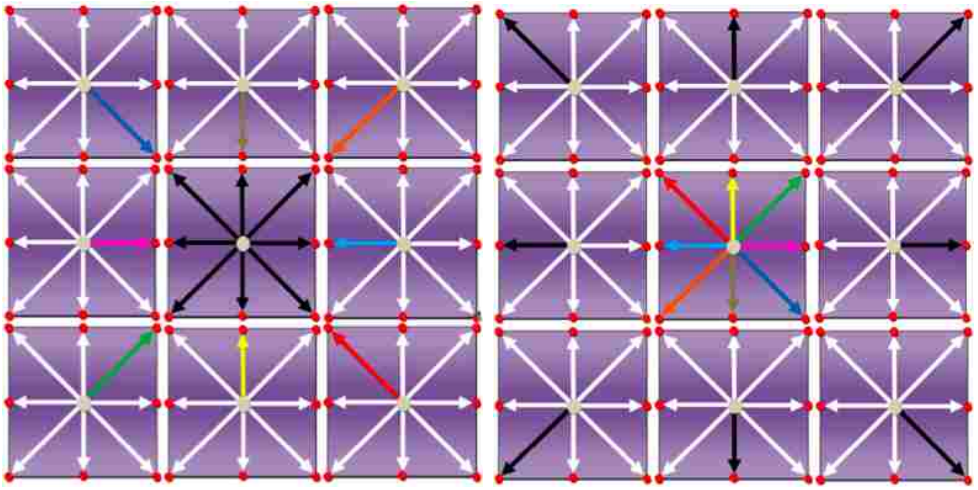

(a) Pre-particle streaming. (b) Post-partcle streaming.

Figure 3.2: Particle streaming between nodes. The distribution functions of the node in the center, represented by black arrows are streamed to neighboring nodes, along the same direction. Correspondingly, the colored distribution functions of the neighboring nodes are streamed to the center node, along the same direction.

to have numerical instabilities at high Reynold's number (Latt 2011), (Mei et al. 2000) and (Feichtinger 2005). The D3Q27 has particles streaming to the 8 corners of a cubic lattice, in addition to the 19 directions of the D3Q19 model. It has all the advantages of the other two models but requires more computations per iteration while authors have reported that it's simulation results are not too different from the D3Q19 model at high flow conditions (Mei et al. 2000), (Habich 2006), (Feichtinger 2005) and (Latt 2011).

The basic LBM algorithm consists of two steps; Particle streaming and collision.

Streaming: This step involves the transfer of the particles between nodes along a particular velocity direction as depicted in the transfer of the colored particles in Fig. 3.2. Mathematically, it is given as

$$f_\alpha(\vec{x} + \vec{e}_\alpha \partial t, t + \partial t) = f^*_\alpha(\vec{x}, \vec{e}_\alpha \partial t) \tag{3.3}$$

Collision: During this step, momentum exchange between the particles take place due to collision with each other at a particular node according to;

$$f_\alpha^*(\vec{x}, \vec{e}_\alpha \partial t) = f_\alpha(\vec{x}, \vec{e}_\alpha \partial t) + \Omega \tag{3.4}$$

$f_\alpha^*(\vec{x}, \vec{e}_\alpha \partial t)$ is the post collision distribution function, $f_\alpha(\vec{x}, \vec{e}_\alpha \partial t)$ is the pre-collision distribution function and Ω is the collision operator. The collision operator accounts for the fact that after collision, the total number of particles in a node along a particular direction changes due to momentum exchange between the particles.

These two steps are combined with appropriate internal and external boundary conditions to obtain the macroscopic variables of density and pressure as moments of the particle distribution functions.

$$\rho(\vec{x}, t) = \sum_0^{18} f_\alpha(\vec{x}, t) \tag{3.5}$$

$$\vec{u}(\vec{x}, t) = \frac{1}{\rho(\vec{x}, t)} \sum_0^{18} \vec{e}_\alpha f_\alpha(\vec{x}, t) \tag{3.6}$$

3.2 Kinetic Models

Bhatnagar-Gross-Krook (BGK) and Multiple Relaxation Time (MRT) models will be used to approximate the collision term (Struchtrup 2005) and (D'Humieres et al. 2002). In the BGK approximation, particle distribution evolves due to collision tending toward an equilibrium distribution function which is defined by the macroscopic velocity at that particular point. The collision term in the BGK model is given by;

$$\Omega = \frac{1}{\lambda}[f_\alpha(\vec{x}, \vec{e}_\alpha \partial t) - f_\alpha^{eq}(\vec{x}, \vec{e}_\alpha \partial t)] \tag{3.7}$$

$f_\alpha^{eq}(\vec{x}, \vec{e}_\alpha \partial t)$ is the equilibrium distribution function which is obtained from the macroscopic values of the velocity and density as given below,

$$f^{eq}(\vec{x}, t) = w_\alpha \rho(\vec{x}, t) \left[1 + 3\vec{e}_\alpha \vec{u} + 9\frac{(\vec{e}_\alpha \vec{u})^2}{2} - 3\frac{\vec{u}^2}{2}\right] \tag{3.8}$$

w_α is the weight factor for the α velocity direction while ρ and u are the macroscopic density and velocity respectively, all in lattice units. For Equation 3.7, λ is the dimensionless relaxation time parameter and it measures the rate at which the distribution functions tend towards equilibrium. Thus, collision is considered a relaxation process that evolves toward an equilibrium state since the value of the new distribution function is modified based on its deviation from the equilibrium function. It is also a tuning parameter that controls the viscosity of the fluid and hence, the flow Re, as given in Equation 3.9.

$$\nu_{lu} = \frac{(2\lambda - 1)}{6}; \qquad \lambda > 0.5 \tag{3.9}$$

A single relaxation rate for all variables in the BGK model leads to significant instability when fluids with low viscosities are simulated. It also limits the range of fluid physical parameters that can be modeled. In contrast to the BGK model, the multiple relaxation time (MRT) model developed by D'Humieres et al. (2002), independently adjusts the rate at which the individual variables relax due to collision, towards equilibrium. The MRT model has all the typical features of a lattice Boltzmann method except that it deals with moments of the distribution function since the moments provide a convenient way of expressing the various relaxation processes due to collision.

Collision in the MRT method is represented by a generalized relaxation process in which the distribution functions for the different velocity directions approach their local equilibrium values at different characteristic time scales given in terms of a collision matrix, **S**.

$$\Omega_{\alpha|(x,t)} = -\mathbf{S}\Big(f_\alpha(\vec{x},t)\big) - \big(f_\alpha^{eq}(\vec{x},t)\Big) = -\sum_\beta S_{\alpha\beta}\Big(f_\alpha(\vec{x},t) - f^{eq}(\vec{x},t)\Big) \tag{3.10}$$

$S_{\alpha\beta}$ are elements of the collision matrix whose eigenvalues are the inverse of the relaxation times for the different processes. Thus all the eigenvalues must be between **0** and **2**. The BGK method is equivalent to the MRT model when all the elements of the collision matrix are the same. The streaming process, like in other LB methods, proceeds in the phase space. However, collision is designed to take place in the moment space since some moments of the distribution functions represent physical phenomena, like density, momentum, viscous stress. This requires a transformation from the velocity space spanned by the distribution functions to the moment space spanned by the moments of the distribution functions, and the transformation matrix comprises of linear set of vectors that are orthogonalized by the Gram-Schmidt procedure. The MRT LBE

$$f_\alpha(\vec{x} + \vec{e}_\alpha \partial t, t + \partial t) - f_\alpha(\vec{x},t) = -\mathbf{M}^{-1}\hat{S}\left[m_\alpha(\vec{x},t) - m_\alpha^{eq}(\vec{x},t)\right] \tag{3.11}$$

is obtained using the transformation

$$m_\alpha = \mathbf{M} f_\alpha; \qquad f_\alpha = \mathbf{M}^{-1} m_\alpha \tag{3.12}$$

M is the transformation matrix constructed as polynomials of the discrete velocity components.

According to the MRT method, the eigenvectors of the collision matrix **S** are the column vector components of the transformation matrix so that using the spectral theory for matrix diagonalization, a diagonal collision matrix, $\hat{S}$ in moment space, is obtained from which the kinematic and bulk viscosities of the fluid can be obtained. The elements of the collision matrix will be chosen as recommended by D'Humieres et al. (2002). The values are also the MRT implementation in OpenLB and Palabos.

3.3 Sources of Error

In LBM, spatial truncation errors do not arise from the approximation of the flow equation like in other numerical methods, since the fundamental equation, the LBE is a discrete form of the Boltzmann equation. Errors, however, are due to the approximation of the real porous media and when the limits of application of the LBE are surpassed as outlined below.

3.3.1 Finite Size effect

The finite size effect is determined by the Knudsen number which is the ratio of the mean free path to the characteristic dimension of the pore spaces. These effects are the major sources of error in the LBM and are caused by insufficient grid points in the lattice to resolve the small pores in the domain. The accuracy of LBM simulation results increases with decreasing Knudsen number i.e large computational domain size, and meeting this requirement is a major challenge especially for low porosity reservoirs rocks with very small connected pore spaces (percolating pore space). This type of systems may require unreasonably large computational size to properly resolve the percolating pore spaces. Thus, this effect limits the extent of application of the LBM for real porous media with tight pores like in fractured carbonates. To quantify the extent of the finite size effect, simulation is performed at different resolutions and the estimated permeability is compared to analytical and/or experimental results. Finite size effect can be minimized by using smaller values of relaxation times (Zou

and He 1997) and (Okabe 2004). However, at very low relaxation time values, especially close to 0.5, the LB algorithm becomes unstable.

3.3.2 Compressibility effects

As earlier stated, the LBM assumes fluid to be in a weakly compressible state as evident in the equation of state given in Equation 3.21. The compressibility is measured by the Mach number.

$$Ma = \frac{\text{Mean speed of fluid}}{\text{speed of sound}} \tag{3.13}$$

And for the lattice system

$$Ma = \frac{u}{c_s} \tag{3.14}$$

To use the LBM for incompressible flow simulation, it is necessary to reduce the lattice fluid compressibility by minimizing the Mach number. It is important to note that this Mach number is not the physical number that relates to the speed of sound in air. Rather, c_s (lattice speed of sound) is the speed with which information is transfered through the model while the Mach number in Equation 3.13 represents the upper limit of the lattice velocity to simulate weakly compressible flows. The recommended Mach number is 0.1 (Timm Kruger 2009) and this limits the average lattice velocity in the system to about 0.057. Mean velocities beyond this value a creates a greater dependence of pressure on density and produces pressure oscillations that prevents flow simulations from converging.

3.3.3 Discretization

This error is due to the inability of the regular lattice to accurately reproduce the geometry of the pore spaces. LBM uses regular lattices to discretize the computational domain and as such creates roughness in the form of stair cases on the boundaries of pore and rock

matrix. The result is that particle bounceback does not take place on the actual pore/matrix interphase but on solid nodes adjacent adjacent to fluid nodes. This effect can be minimized by also increasing the lattice resolution since smaller voxels will improve the delineation of the boundaries by the nodes.

3.4 Lattice Units and Unit Conversion

In LBM, parameterized values of the lattice constants and fluid/flow properties in lattice units are used in simulation and the correspondence between the real physical system that is being simulated and the parameterized simulation is achieved through the Reynolds number (principle of dimensional similarity). Important lattice constants used for relating measurements in the two systems are the resolution, discrete time step and the viscosity in lattice units. However, in OpenLB/Palabos, an additional unit known as the dimensionless system is introduced to interface between the lattice units and the physical units. This has the advantage that from the dimensionless units, the simulation result can be related to any physical system of arbitrary value. Using Darcys law and appropriate unit conversion between the physical units and the lattice unit, the components of the permeability tensor of the system are calculated as will be shown in Sec. 4.4.

The basic unit conversions used in the LBM for single phase flow are given below, where all the flow variables are functions of time and are defined at every lattice node.

$$\Delta x = \frac{L}{N_i} \tag{3.15}$$

$$u_p = u_{lu}\frac{\Delta x}{\Delta t} \tag{3.16}$$

Using the maximum lattice velocity from the Mach number limit, the maximum simulated velocity in physical units is

$$u_{p_{max}} \approx 0.057 \frac{\Delta x}{\Delta t} \tag{3.17}$$

$$\nu_p = \nu_{lu} \frac{\Delta x^2}{\Delta t} \tag{3.18}$$

$$Re = \frac{\rho_p u_p D_p}{\mu_p} = \frac{u_{lu} D_{p_{lu}}}{\nu_{lu}} \tag{3.19}$$

$$p_p = p_{lu} \rho_p \frac{\Delta x^2}{\Delta t^2} \tag{3.20}$$

Δx= lattice resolution, Δt = time step, L = physical length of the domain in i direction and N_i = lattice size in i direction.

In addition, fluids in LBM are treated as weakly compressible with an equation of state given below.

$$p_{lu} = c_s^2 \rho_{lu}; \qquad c_s^2 = \frac{1}{3} \tag{3.21}$$

p: pressure, ρ=fluid density, c_s = lattice speed of sound.

Combining of Equations 3.20 and 3.21 gives

$$p_p = \rho_{lu} c_s^2 \rho_p \frac{\Delta x^2}{\Delta t^2} \tag{3.22}$$

3.5 OpenLB and Palabos

The open source code OpenLB is a numerical framework for lattice Boltzmann simulations that can implement both serial and in parallel computations using either MPI or OpenMP (Latt 2008). It scales well over thousands of cores even with small lattice sizes. During each

* Subscripts: p:physical units; lu:lattice units

iteration, the code calculates both collision and propagation of the distribution function. Using this package, it is easy to reach regimes in which billions of lattice sites are processed in one second. Thus, code performance is measured in lattice updates per second and it represents the number of lattice sites that complete a collision and propagation cycle in one second. Units are **lus**, **Mlus** (Mega-lus), **Glus** (Giga-lus). Palabos is the latest release of OpenLB and it has better parallelism with capability to implement more LBM models both for single phase and two phase flows. Scaling studies of OpenLB is presented in Sec. 5.1.

3.6 Resources

Image volume files (IVF): IVF is the input to the simulation and is essentially an ASCII file that contains the characters 1 and 0 which describe the pore and matrix phases distribution of the rock samples.

OpenLB: The LBM algorithm will be implemented using OpenLB. OpenLB is able to simulate incompressible single phase and multi-phase flow dynamics using popular kinetic models like BGK and MRT to model particle interactions.

Computing platform: In order to capture the secondary flow patterns developed in inertial dominated flows in porous media, a large resolution of the digital porous media is necessary. Thus, a typical simulation of flow on realistic porous media will require over 15 million grid points which is equivalent to over 250 million degrees of freedom using the LBM. To meet computational demand and large memory requirement for these simulations, we use the computer clusters at LSU High Performance Computing (HPC) and some of the Louisiana Optical Network Initiative (LONI) systems. The LSU HPC systems are capable of over 3 Tflops while Queen Bee, LONI's flagship supercomputer is a 50.7 Tflops system at peak performance (LONI 2011).

Visualization packages: To illustrate the tortuous flow paths of the fluid particles through the complex pore structure of the rock samples, we shall use the open source Paraview and/or the commercial Ensight and Avizo packages respectively to visualize the image file output from OpenLB or Palabos.

Chapter 4
Modeling and Simulation Methodology

4.1 Approach

Fluid flow in reservoirs, whether in Darcy or inertial dominated regimes, is driven by pressure gradient prevailing around the wellbores. We shall simulate such pressure-driven flow in the 3-D models of reservoir rocks, as provided in the image volume files, to estimate the flow and rock parameters using the lattice Boltzmann method on high performance computing resources. This procedure is summarized as shown in the flow chart of Fig. 4.3.

Two approaches will be used to impose the pressure gradient on the media:

1. Density difference approach: In this approach, the pressure gradient to drive flow in the porous media is implemented by imposing fluid density gradient in the direction of flow by using Equations 3.21 and 3.22. As a result, the pressure gradient in physical units is related to the lattice units value by

$$\left(\frac{\Delta p}{L}\right)_{i_p} = \rho_p \frac{\Delta x}{\Delta t^2} \left(\frac{\Delta p}{L}\right)_{i_{lu}} \tag{4.1}$$

Where

$$\left(\frac{\Delta p}{L}\right)_{i_{lu}} = \frac{\Delta \rho_{lu}}{3N_i} = \frac{\rho_{inlet} - \rho_{outlet}}{3N_i} \tag{4.2}$$

Thus, equation (4.1) becomes

$$\left(\frac{\Delta p}{L}\right)_{i_p} = \rho_p \frac{\Delta x}{\Delta t^2} \frac{\Delta \rho_{lu}}{3N_i} \tag{4.3}$$

2. Body force approach: In this approach, pressure gradient is imposed on the fluid in the domain by using a uniform body (b_{f_i}) force added at each time step to the fluid particles in the pore space. The body force produces the same amount of flow as the pressure driven flow since its value is calculated from the pressure gradient.

$$\left(\frac{\Delta p}{L}\right)_{i_{lu}} = b_{f_i} \tag{4.4}$$

The particles are accelerated at each time step by addition of this force to the distribution functions in the direction of the imposed pressure gradient while a corresponding amount of the body force is subtracted from particles moving in the opposite direction. The equivalent pressure gradient is calculated using Equation 4.1.

4.2 Initial Conditions

The initial state of the system is only important when a time dependent flow is studied. To calculate the flow parameters, the final steady state for a particular driving force is desired and is independent of the initial conditions. Thus, to speed up the simulation, an initial velocity distribution of 0.01 lu will be defined over the whole domain. Since the LB method works with the distribution functions, the defined macroscopic velocity will then be transformed into the corresponding particle distribution functions which are used as the initial values for simulation.

$$\vec{u}(\vec{x}, t) = U_{ini} \tag{4.5}$$

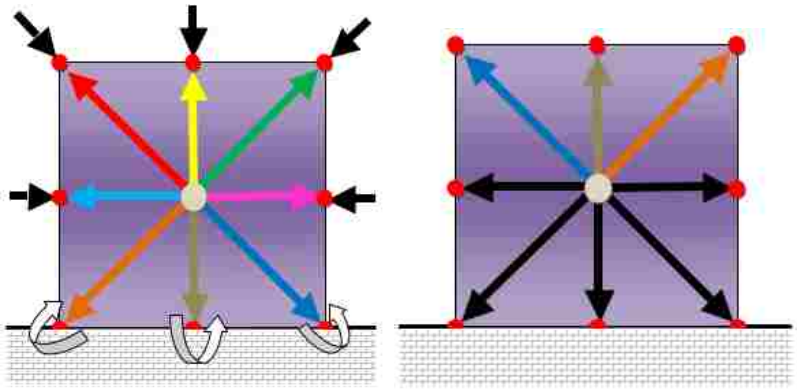

(a) Particle distributions before bounce back.

(b) Partcle distribution after bounce back.

Figure 4.1: 2D representation of particle bounce back around the pore-solid boundary. Particles next to the solid boundaries, traveling into the solid phase are bounced back and streamed in the opposite direction, into the fluid.

U_{ini} is the value of the lattice velocity initialized on all lattice nodes of the computational domain. A value of 0.01 was used in this work for all flow simulations.

4.3 Boundary Conditions

No slip boundary condition at the fluid/solid interface will be implemented using the standard bounce back scheme illustrated in Fig. 4.1. In this scheme, the distribution function traveling from a fluid node to a neighboring solid node is bounced back along the same link. This ensures a zero velocity vector on the bounce back node as obtained in real fluid flows. Fluid flow will be open to domain faces perpendicular to the direction of the imposed pressure gradient while faces parallel to flow directions will be sealed with no flow boundaries. This is done to mimic the experimental setup used for flow simulation in the laboratory. However, for periodic domains, periodic boundary condition will be used on all the external faces such that the distribution function leaving a particular boundary face renters the domain on the opposite boundary, along the same link.

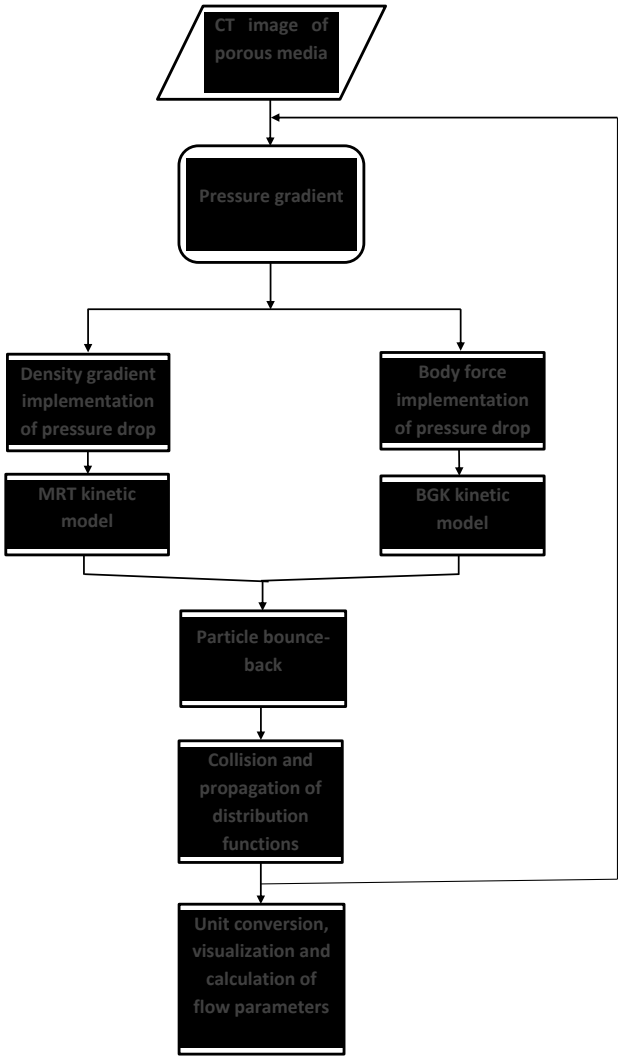

Figure 4.2: Summary of LBM procedure for porous media simuation

4.4 Estimating Flow Parameters

4.4.1 Scaling Study and Parameter Tuning

The results will be analyzed to investigate the effect of relaxation time and resolution on the permeabilty and non-Darcy coefficient. The relaxation time that gives a permeability estimate close to the experimental value at a reasonable computational domain size will be used for further analysis for the particular sample.

In the following section, the porous media macroscopic variables of interest will be outlined and the techniques of obtaining them from the LBM variables and simulation results will be given.

4.4.2 Porosity

Porosity of a medium is given by the ratio of the total number of voxels with a value of 0 assigned to the centre, to the total number of voxels in the domain.

$$\phi = \frac{\text{volume of pore space}}{\text{bulk volume}} = \frac{\sum I(\vec{x}) = 0}{\prod N_j} \tag{4.6}$$

4.4.3 Tortuosity

Tortuosity is a lineal measure of the complex pathways in the pore spaces and is estimated using the two Equations below, which are variations of the equations suggested by Nabovati and Sousa (2007).

$$\tau = \left(\frac{\sum u_{mag}}{\sum |u_j|} \right)^2 \tag{4.7}$$

$$\tau_1 = \left(\frac{\sum u_{mag}}{\sum u_j} \right)^2 \tag{4.8}$$

Since negative values of velocity component in the direction of pressure gradient will be expected, the tortuosity values obtained from Equation 4.8 will be larger than those obtained from Equation 4.7 due to the fact that the effect of negative velocities on the denominator is to reduce the over all summation, and hence, increase the ratio as compared to Equation 4.7 where the summation is over the magnitude of the velocity in the direction of applied gradient.

4.4.4 Permeability

On converting the variables in Darcy's law to lattice units, Equation 4.9 is obtained and used to calculate the components of permeability for periodic and irregular domains.

$$k_{ij} = \frac{\Delta x^2 \nu_{lu} u_i}{(\Delta p / L)_{j_{lu}}} \tag{4.9}$$

4.4.5 Beta factor

The beta factor is obtained as the slope of the plot of the inverse of the apparent permeability versus the pseudo Reynolds number as presented in the Equation 4.10, where the intercept on the inverse apparent permeability axis provides an estimate of the intrinsic permeability of the medium.

$$\frac{1}{k_{app}} = \frac{1}{\mu \langle u \rangle} \frac{\Delta p}{L} = \frac{1}{k_{int}} + \frac{\beta \rho \langle u \rangle}{\mu} \tag{4.10}$$

4.5 Porous Media Cases Studied

4.5.1 Regular and Random Sphere Packs

The porous media, shown in Fig. 4.5 will be used to validate the method. The first medium consists of a distribution of uniform spheres in a body centered cubic arrangement. The length of the cube is 175 μm. The second is the CT image of a real porous media. It consists of irregular distribution of 123 μm diameter spheres in a cube. The tomography image is discretized into $250 \times 250 \times 250$ voxels with a resolution of 5.8 μm at 40.7% porosity. For these type of media, flow distributions have been extensively studied and analytical and empirical expressions for their flow parameters abound.

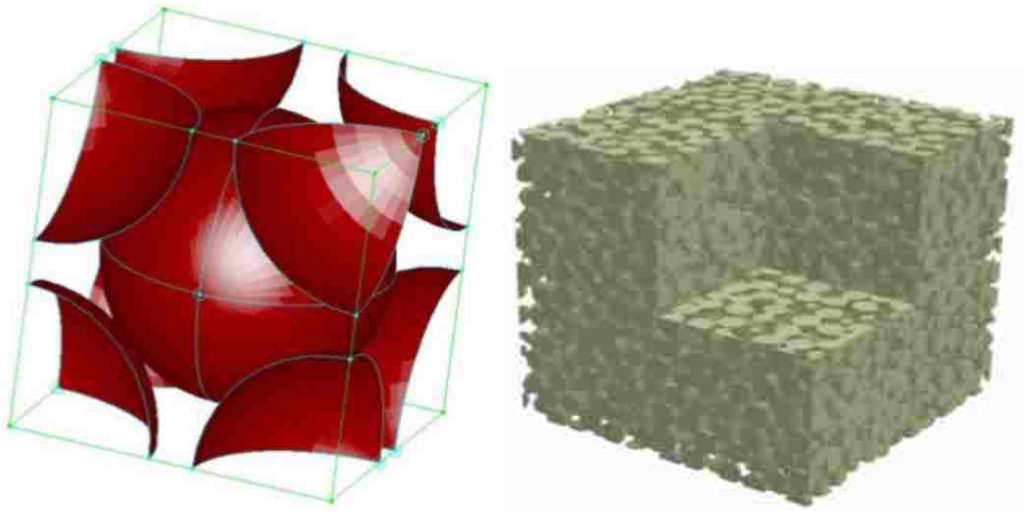

(a) Regular BCC (b) Irregular packing

Figure 4.3: Sphere pack porous media

4.5.2 Castlegate Sandstone

The castlegate sandstone is the second oldest of the several sandstone formations within the cretaceous Mesaverde group of east-central Utah. The formation analyzed is an outcrop rock of approximately $150 - 180$ μm grains of which about 70% are quartz and the remaining 30% includes rock fragments, feldspar and mica. Although the formation contains very small amount of original clays, much of the pristine rock fragments are altering or have altered to clays and are at various stages of deformation between the compact rock grains like quartz. Images of the rock sample obtained from thin sections and SEM highlighting some of the features outlined above are shown in the figures below. In addition, the porosity of the sample is reported as 21-25% and it comprises interparticle, intraparticle and secondary porosities. Intraparticle pore spaces are found within the rock fragments and are thought to form due to deformation, dissolution and alteration of original rock fragments to clay.

Imaging and Segmentation

A 3-D image of the sample for numerical simulation was obtained by micro-tomography imaging of a 6 mm sample of the castlegate. During the procedure, the sample was exposed

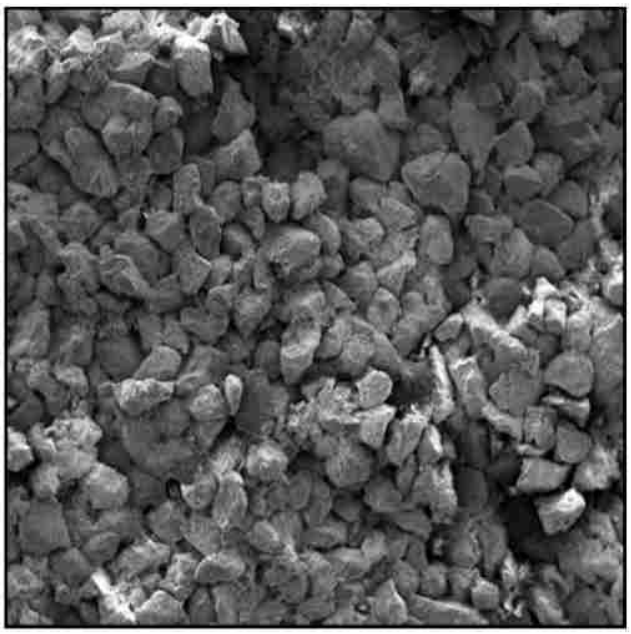

Figure 4.4: SEM. Shows well sorted grains with minor coatings of clay. Inter particle pore space is very well connected.

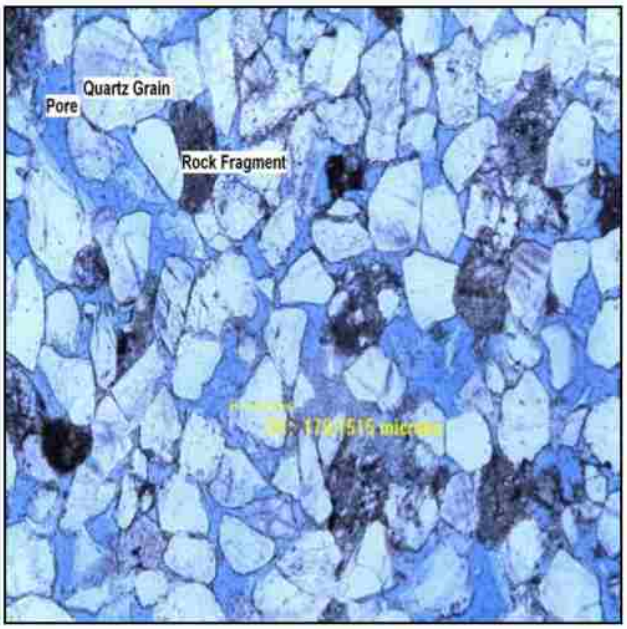

Figure 4.5: Thin-Section. White grains are primarily quartz and igneous rock fragments and dark grains are shale or rock fragments.

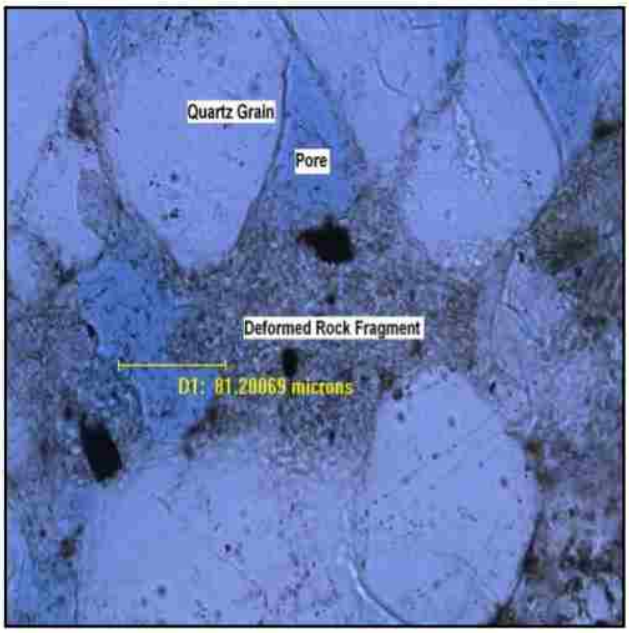

Figure 4.6: Thin-Section photomicrograph. Ductile rock fragment has been deformed between quartz grains, reducing the inter-particle porosity.

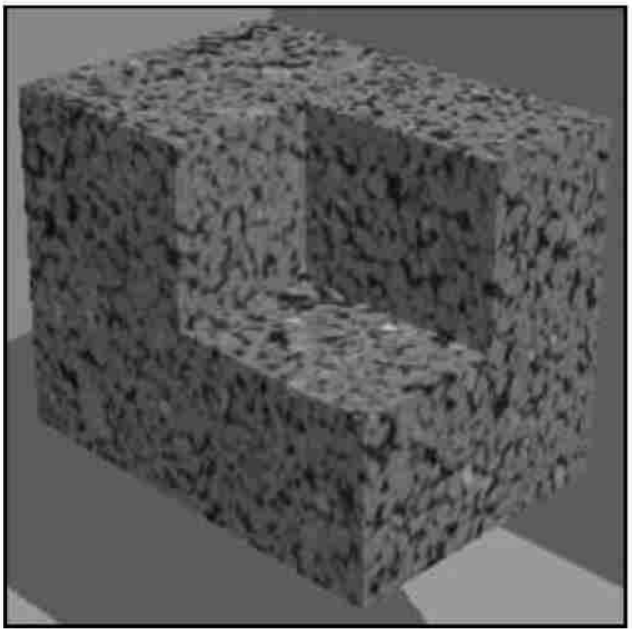

Figure 4.7: Constructed 3D gray scale image of the Castlegate sandstone.

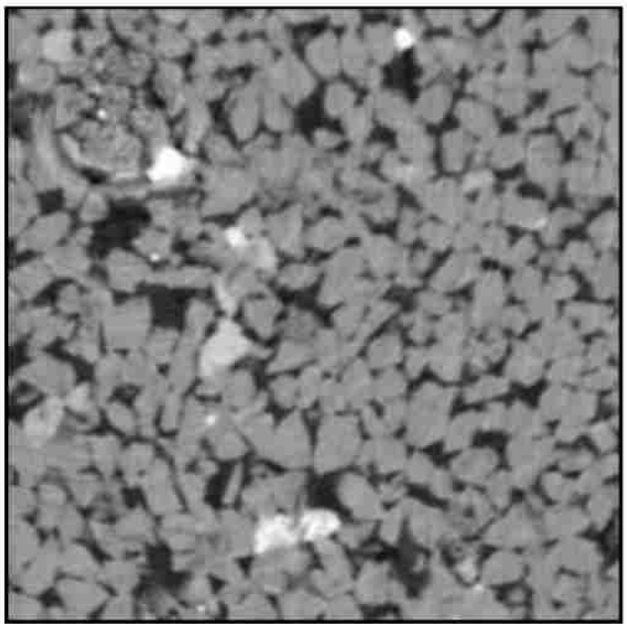

Figure 4.8: 2D slice (150 of 425) of gray scale image.

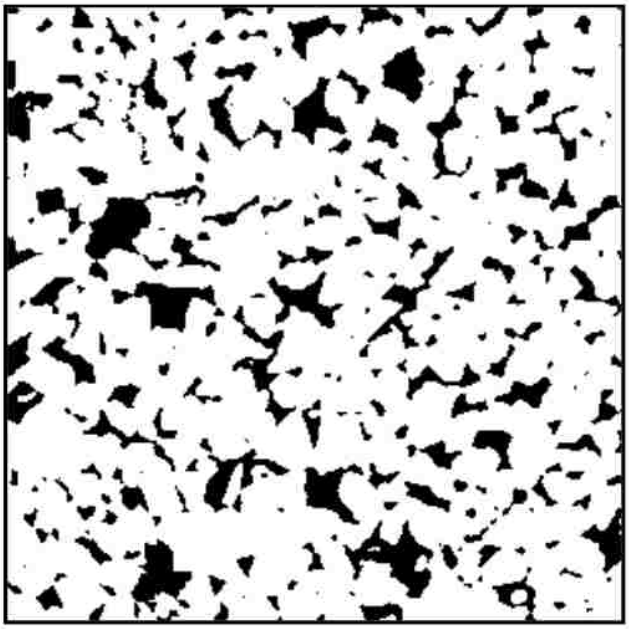

Figure 4.9: 2D slice (150 of 425) of the segmented gray scale image, showing clearly pore spaces (black) and the rock matrix (white).

to a 30 keV X-ray energy source for 1.5 secs and threshold values of $90, 100$ on the gray scale were used to segment the reconstructed image into solid and void spaces respectively using a target porosity of 20%. A $300 \times 300 \times 425$ voxels subset with resolution of 7.57 μm, corresponding to $2.271 \times 2.271 \times 3.217$ mm of the original sample was cut off from the imaged sample for further analysis. Figs. 4.7, 4.8 and 4.9 show the original gray scale and segmented images respectively, of the analyzed sample.

The computational domain is obtained by defining its nodes at the center of the voxels of the segmented image. In this work, a cubic subset of size $300 \times 300 \times 300$ voxels of the original imaged sample is used as the simulation domain. The domain is discretized using the indicator function of Equation 2.14 to describe the phase distribution on the nodes, where the distance between two nodes (7.57 μm) is the image resolution or voxel size.

* CT imaging of the Castlegate Sandstone was carried out by Dr. Clinton Willson (cwillson@lsu.edu) while petrophysical analysis was done by Dr. Stephen Sears (sosears@lsu.edu)

Chapter 5
Results and Discussion

5.1 Code Performance and Scalability

The performance of the OpenLB code used for our simulation is tested by running on a number of cores on the high performance computing (HPC) resources at Louisiana State University (LSU) and noting the wall clock time it takes to execute a fixed number of iterations. The I/O operations were reduced to minimize the time spent by the processors in writing out image and data files. Strong scaling results and efficiency of the OpenLB code for the 250^3 irregularly arranged sphere pack computational domain on the HPC systems are shown in Figs. 5.1 and 5.2 respectively. Fig. 5.1 shows a significant decrease in execution time as more cores are used in running the code. Beyond 56 - 64 cores, the benefit of using more processors for simulating flow on the 250^3 computational domain diminishes as significant time saving was not gained by running on more nodes. This is supported by the curve tending towards an asymptotic value at higher processor counts. Efficiency measures the speed of code execution with increasing number of cores, and for an ideal system, (i.e 100% efficiency), a linear relationship should be maintained between execution speed and number of cores. In Fig. 5.2, the code performance deviates from the initial linear relationship as more nodes are added to the communication domain. Beyond the linear regime, the speed of execution does not scale up with the increasing number of processors and this corresponds to the diminishing execution speed observed in Fig. 5.1.

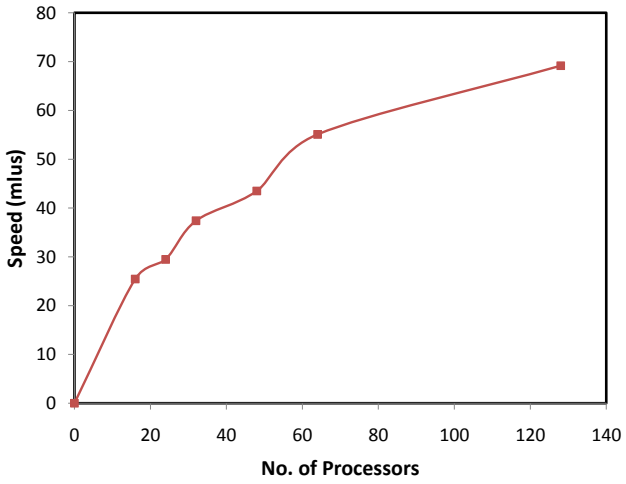

Figure 5.1: Scaling of OpenLb over multiple processors.

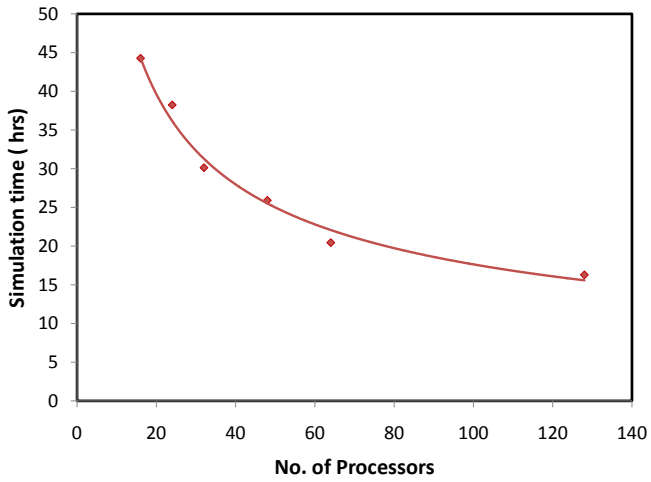

Figure 5.2: .
Efficiency of HPC systems.

5.2 Verification and Validation Cases

5.2.1 Body Centered Cubic (BCC) Sphere Pack

Flow was simulated in the media represented by Figs. 4.3a until steady state was reached. Using Equations. 4.7 and 4.8, two estimates of the average tortuosity are calculated at different Re while the components of the permeability tensor are obtained from the simulation results at low values of average velocity for which Darcys law is valid. Since the domain geometry is periodic with respect to its boundaries, the diagonal components of the tortuosity, permeability and beta factor respectively for the BCC sphere pack will be the same while the off-diagonal components will be zero.

Like in all numerical methods, the LBM simulation results are dependent on the resolution of the computational domain which, for porous media, determines the physical accuracy in representing pore boundaries using voxelized images. We quantified the effect of lattice resolution on our simulation by varying the size of the computational domain for the regular BCC distribution of spheres and calculating the permeability from the simulation results. In addition to resolution, the relaxation rate of the distribution function, specified by the re-

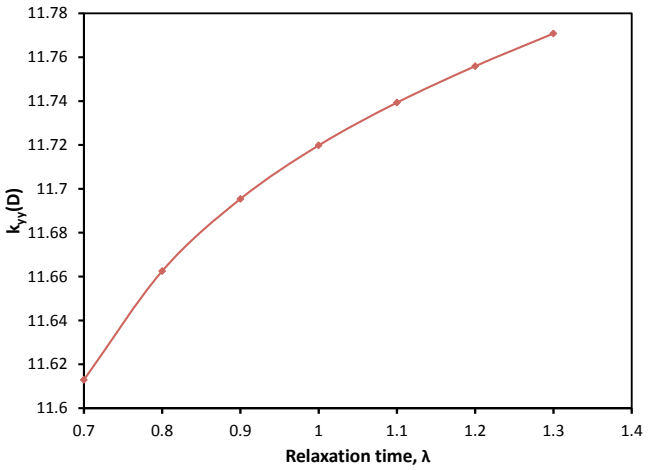

Figure 5.3: Permeability variation with relaxation time for regular BCC sphere packing.

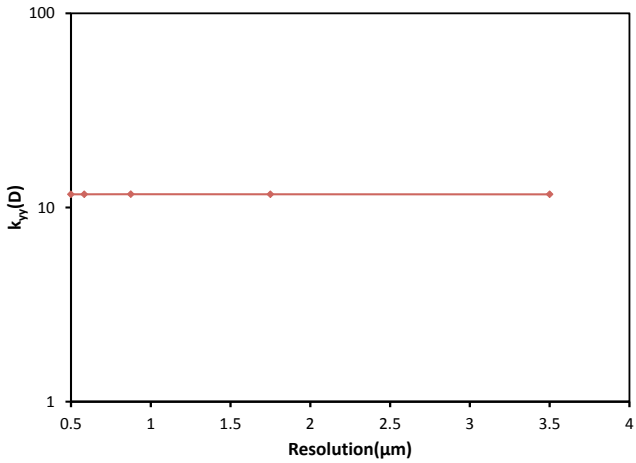

Figure 5.4: Permeability variation with resolution for regular BCC sphere packing.

laxation time also affects the simulation result since it determines the location of the bounce back nodes on the interphase between the pore and the rock phases. Thus, the relaxation rate is varied for a fixed resolution (350^3 size) at $Re \approx 0$ and the response of calculated **y**-direction permeability is plotted as shown in Fig. 5.3. The graph shows decreasing apparent permeability trend at decreasing values of the relaxation times analyzed. The change, however, is small with 1.35% change between the maximum and minimum values. Thus, for this domain with uniform geometry, the simulation results can be considered to be independent of relaxation time. For further simulations, a relaxation time of 0.9 was used since it guarantees more accurate flow results. Fig. 5.4 shows the plot of permeability in the **y**-direction obtained for different resolutions of the computational domain. On this log plot, the change in permeablity is insignificant with about 0.145% difference between the values obtained for resolutions corresponding to 400^3 and 50^3 computational sizes respectively. This means that the different resolution levels outlined on the graph were adequate to resolve the pore spaces and produce reliable LBM simulation results. To simulate high Re flows and reduce computational times, 350^3 lattice size was used for further simulations. The maximum ob-

tainable Re before the onset of compressibility error (maximum lattice velocity $\approx 0.057\ lu$ at $Ma = 0.1$) for a relaxation time of $\lambda = 0.9$ (lattice viscosity $= 0.1333\ lu$) is given by

$$Re_{max} = \frac{u_{lu_{max}} D_{p_{lu}}}{0.1333}; \qquad u_{lu_{max}} \approx 0.057 \tag{5.1}$$

From the formula above, $Re_{max} = 129$ for the BCC sphere pack at $N = 350$ while the maximum Re simulated in the domain was 83. Again, to ensure accurate simulations, a relaxation time of $\lambda = 0.9$ was used to simulate on the 350^3 lattice size and the permeability estimates obtained were compared with the Carman-Kozeny and Ergun formulae respectively as shown below.

$$K = \begin{bmatrix} 11.7 & 0 & 0 \\ 0 & 11.7 & 0 \\ 0 & 0 & 11.7 \end{bmatrix} D$$

$$k_{\text{Carman}} = 9.23\text{D}$$

$$k_{\text{Ergun}} = 11.08\text{D}$$

The values above show good comparison between the analytical estimates and the diagonal elements of the permeability tensor as obtained from simulation result.

To investigate in detail, the behavior of the permeability and average length of the flow paths in the BCC sphere packing at 350^3 lattice size, the **y**-direction permeability and estimates of tortuosity obtained from Equations. 4.7 and 4.8 are plotted as shown in Fig. 5.5. On the graph, permeability is constant up to $Re \approx 4.0$, beyond which it decreases as Re increases, due to contribution of inertia to high flow regimes. Tortuosity also followed a similar trend as the permeability, with transition occurring at the $Re \approx 4.0$. The region of constant

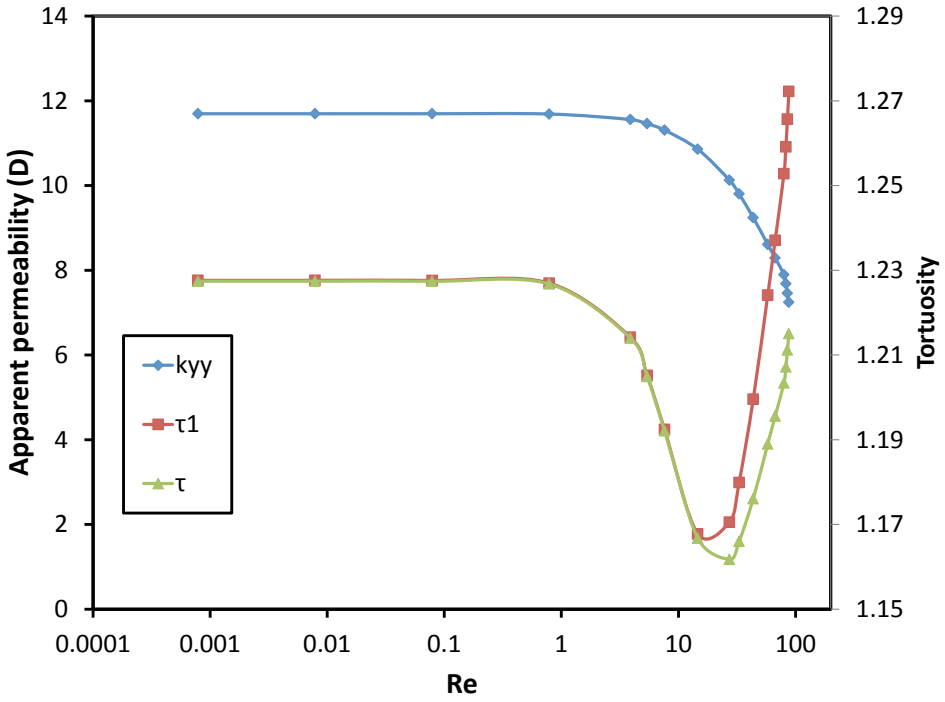

Figure 5.5: Variation of apparent permeability and tortuosity of BCC sphere pack with Re.

permeability and tortuosity signifies the viscous dominated regime for which Darcy's law is valid. In addition, τ is the same as τ_1 at low Reynold's number, but less than τ_1 at high Re as fluid particles recirculate in the domain, in agreement with the explanation of Sec. 4.4.3. However, additional trend in the tortuosity plot is observed as the estimates only decreased till $Re \approx 15$ and $Re \approx 30$ respectively for τ_1 and τ and then increased in value beyond this Reynold's number for τ_1. Below are the tortuosity estimates for the BCC sphere packing at low Re.

$$\tau_1 = \begin{bmatrix} 1.23 & 0 & 0 \\ 0 & 1.23 & 0 \\ 0 & 0 & 1.23 \end{bmatrix} \approx \tau$$

From the result above, we can say that for a unit length of BCC cubic packing, the average length of all the flow paths through the domain is approximately $1.23L$, where L is the flow

domain length.

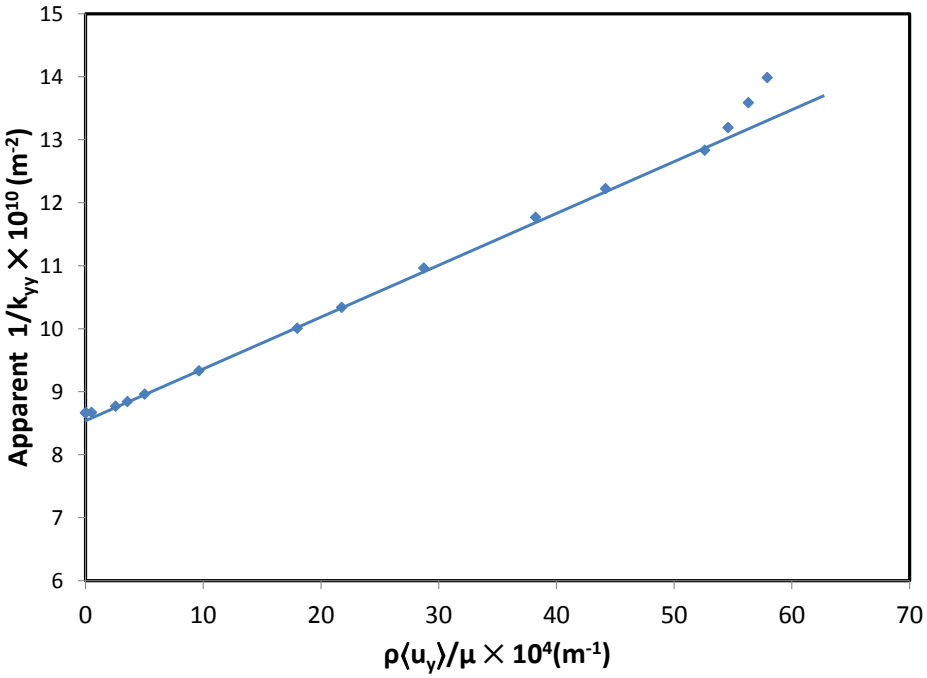

Figure 5.6: Inverse of apparent permeability versus pseudo Re.

To obtain the non-Darcy coefficient in the **y**-direction, the inverse of k_{yy} obtained for different Reynolds numbers were plotted against a pseudo-Reynold's number as shown in Fig. 5.6. In accordance with Equation 4.10, a straight line graph is obtained with intercept equal to the intrinsic permeability while the beta factor was calculated from the slope. It is observed from the graph that, two linear regimes are observed which are here termed the Forchheimer and-post Forchheimer regions respectively. Transition from the Darcy to Forchheimer region occurs at pseudo-$Re \approx 2.6 \times 10^4$ m^{-1} ($Re \approx 4.0$ as earlier shown) while transition from Forchheimer to post-Forchheimer regime occurs at pseudo-$Re = 5.04 \times 10^5$ m^{-1} ($Re \approx 79$). From these linear sections for similar graphs for **x, z**-directions respectively, the diagonal components of the non-Darcy coefficients tensor which are the same for all directions are obtained and presented below.

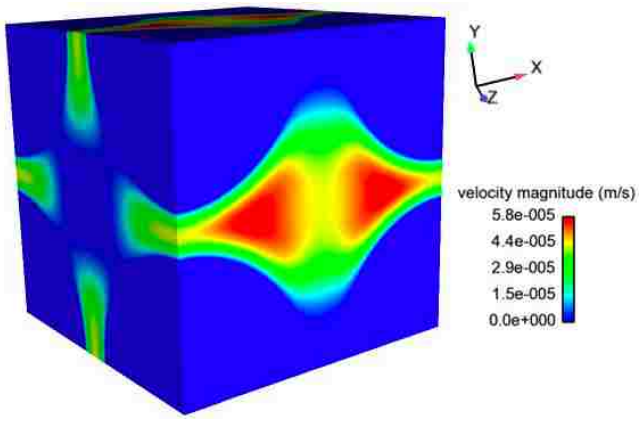

Figure 5.7: Velocity field at $Re \approx 0$.

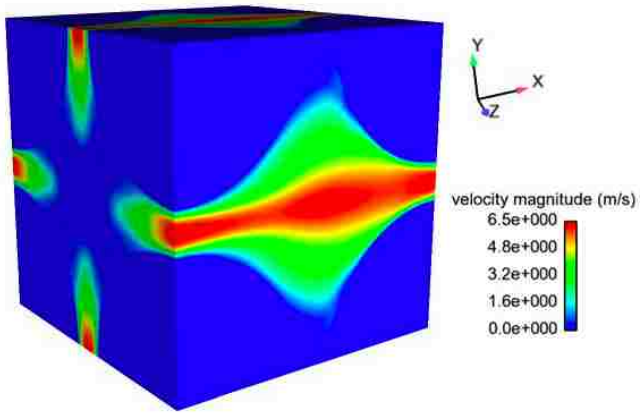

Figure 5.8: Velocity field at $Re = 85$.

$$\beta = \begin{cases} 0; & Re < 4 \\ 75486\text{m}^{-1}; & 4 < Re < 79 \\ 229563\ \text{m}^{-1}; & Re > 79 \end{cases} \tag{5.2}$$

The off-diagonal components of β were obtained as zero because of the periodicity of the domain. In addition, the Ergun estimate of $\beta = 238040\ \text{m}^{-1}$ compares well with non-Darcy coefficient estimated for the linear regime at $Re > 79$.

The steady state velocity fields obtained from simulating flow in the BCC sphere pack at two different Reynold's numbers are shown in Figs. 5.7 and 5.8. In addition, flow streamlines are shown in Figs. 5.9 and 5.10 for low and high Re respectively and characteristic of inertial flows, eddies can be seen behind the particles in the inset of Fig. 5.10 while the streamlines at low Re are parallel to each other, as seen in the inset of Fig. 5.9. These streamlines show the fluid flow direction through all percolation pathways in the domain.

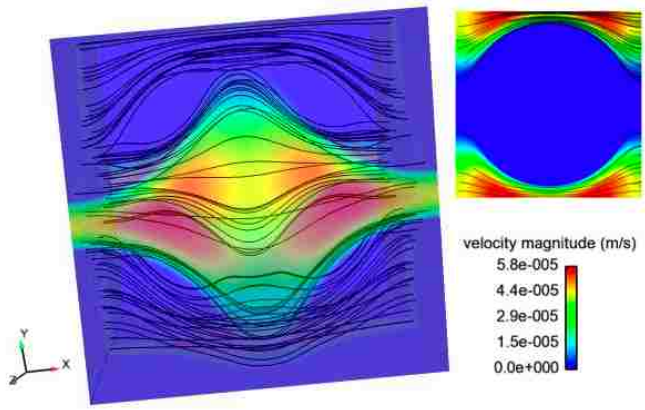

Figure 5.9: Streamlines in BCC sphere domain at $Re \approx 0$.

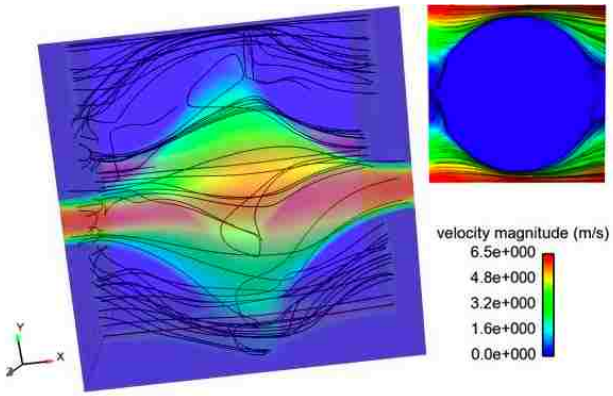

Figure 5.10: Streamlines in BCC sphere domain at $Re = 85$.

5.3 Roughness Studies

In Sec. 5.2, transport properties for the BCC sphere packs were obtained from LBM results at different flow conditions. In carrying out the simulation, the media were assumed to be composed of smooth spheres and this assumption was ideal to obtain results that are verifiable using analytical equations. On the other hand, in addition to the complex nature of the solid-pore interface, porous media in natural systems are characterized by rough interfaces that may impact significantly on the behavior of fluids flowing through them. The formation of these rough surfaces could be the result of deposition of clay and other minerals on the rock matrix, from partial dissolution of the rock matrix, or from fracturing or grain shearing arising from increased overburden pressure. In all of these conditions, the flow parameters will be different from those of the same systems without roughness. Thus, it is important to quantify the effect of grain roughness on flow parameters and how much these parameters deviate from the original systems.

In this section, flow is simulated on a BCC arrangement domain with protrusions on the spheres acting as surface roughness. We modeled the surface protrusions as depositions of hemispherical particles, placed on locations at which planes tangent to the surface of the

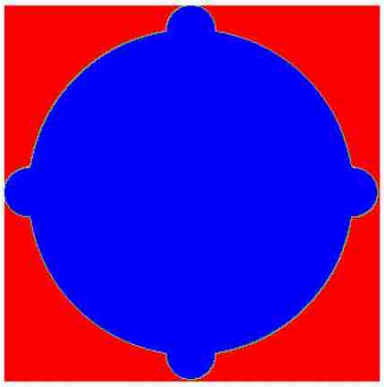

Figure 5.11: 2D representation of roughness on the regular BCC sphere pack.

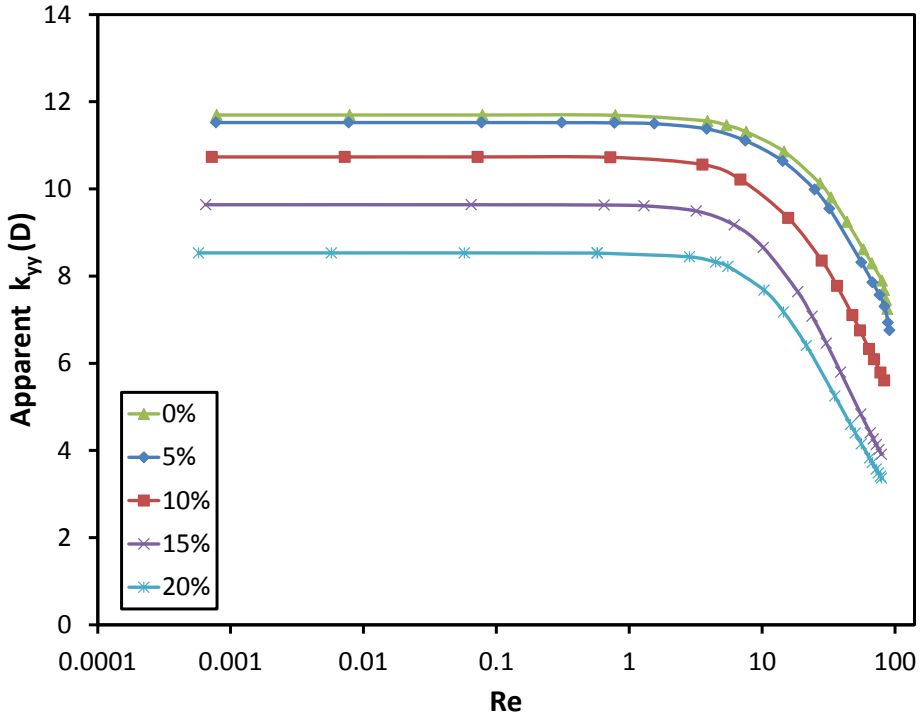

Figure 5.12: Calculated permeability for different roughness domains at different *Re*.

sphere are parallel to the sides of the domain as shown in Fig. 5.11. Six of these protrusions are defined on each sphere and the height is expressed as a percentage of the diameter of the smooth sphere. We simulated for four (4) different roughness heights of $20\%, 15\%, 10\%$ and 5% of the diameter of the sphere and estimated the permeability, tortuosity and beta factor at these roughness conditions. Figs. 5.15 show the flow field through the domain of the rough

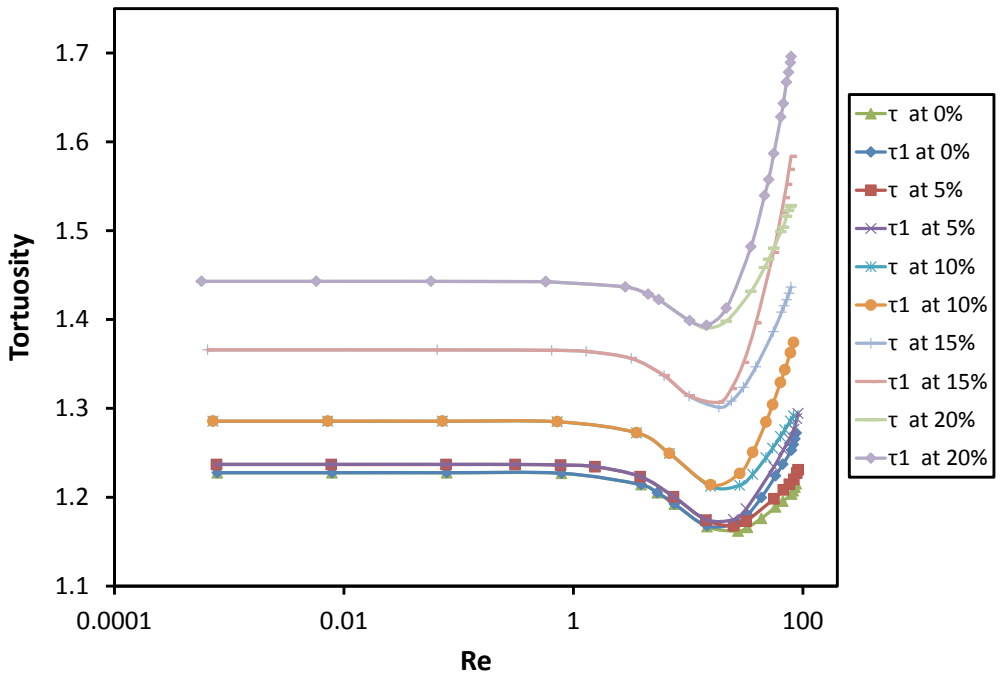

Figure 5.13: τ of different roughness domains at different Re.

spheres, delineating the magnitude of the protrusion as given by their heights. Comparing the streamlines of Figs. 5.16 and 5.17, it is seen that the flow paths through the domain having a roughness height of 20% are more tortuous than those through the 5% roughness height domain. Similar relationship is expected when comparing a domain with larger roughness height to another with smaller roughness height. This is reflected in the plot of tortuosity estimates at different Re for the domains, as shown in Fig. 5.13. At low Re, it is seen from the graph that τ and τ_1 are the same for each individual roughness domain but deviate from each other as Re increases, due to flow path separation which is not considered in the definition of τ. Although the tortuosity trends are similar for flow through all the geometries, the value of the estimates increases with the roughness heights. Thus, the average length of the flow paths through the domain with 20% roughness height is greater than those through the 5% roughness domain. This behavior is further captured in the apparent permeability estimates for the geometries at different Re as shown in Fig. 5.12. Again, the permeability trend for all the domains are the same and similar to that for the smooth sphere. However, the apparent

permeability decreased as the roughness height increased. This finding is closely related to that for tortuosity since larger roughness heights signify greater resistance to flow and hence a corresponding decrease in permeability. In addition, Fig. 5.12 shows that flow deviation from the viscous dominated Darcy regime to the non-Darcy regime occurs within the same Re range ($Re \approx 4.0$) for all the roughness heights and the smooth spheres domain.

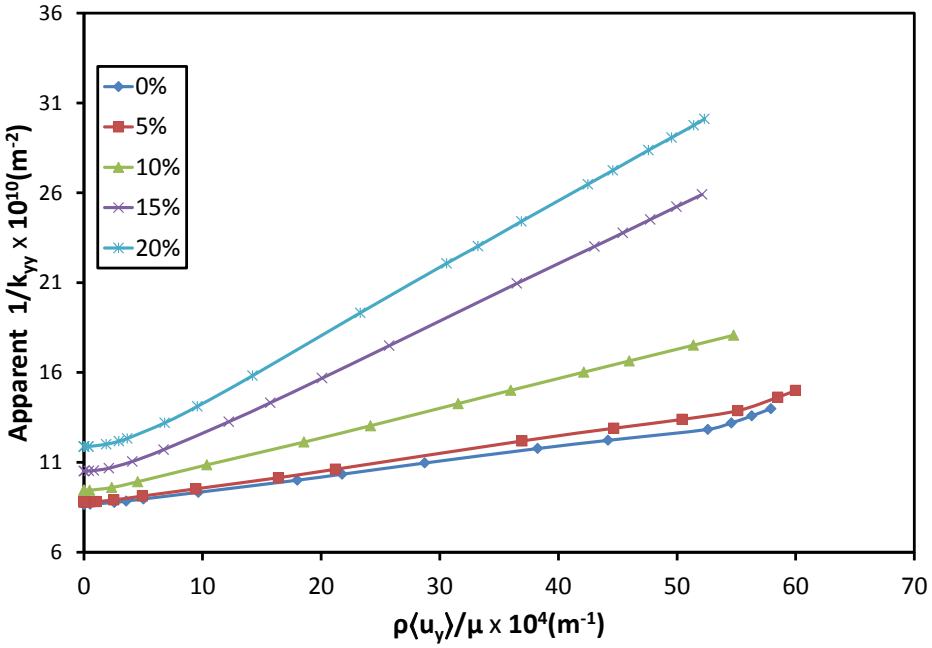

Figure 5.14: Inverse of apparent permeability for different roughness heights.

Finally, from the apparent permeability calculated at different Re from the LBM simulation results, the non-Darcy coefficient was obtained from the plot of the inverse of the apparent permeability versus the pseudo Re. The graph for all the domains is shown in Fig. 5.14 and it is seen that the plots become steeper as the roughness height increases, implying that the beta factor increases. Thus the beta factor increases. This is expected since the greater resistance offered by the larger roughness lengths leads to more contribution by local pressure gradient due to flow inertia increases.

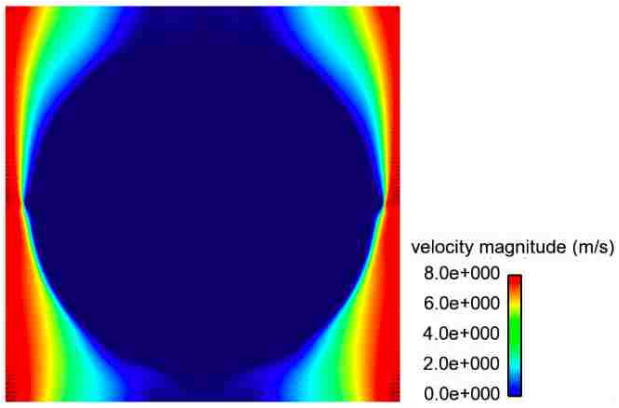

(a) Roughness height = 5%

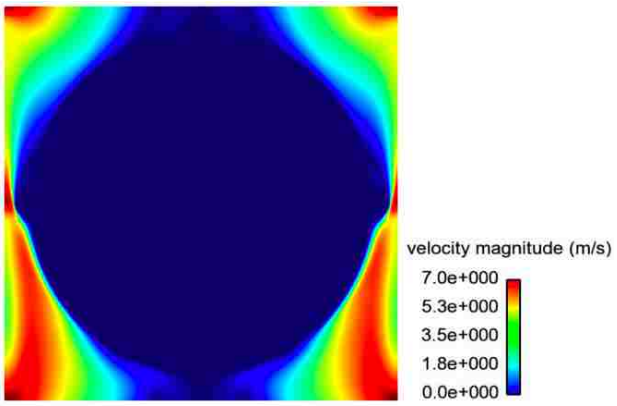

(b) Roughness height = 10%

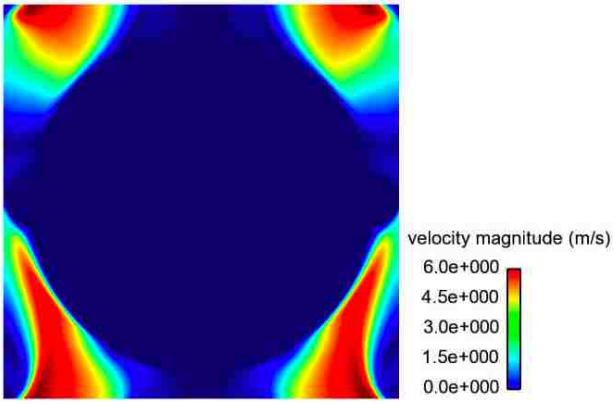

(c) Roughness height = 15%

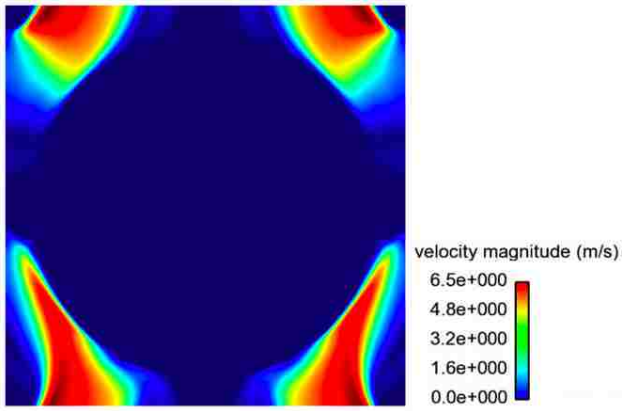

(d) Roughness height = 20%

Figure 5.15: Velocity distribution for flow from bottom to top (**y**-direction) through the rough domains. Roughness height is expressed as percentage of smooth sphere diameter.

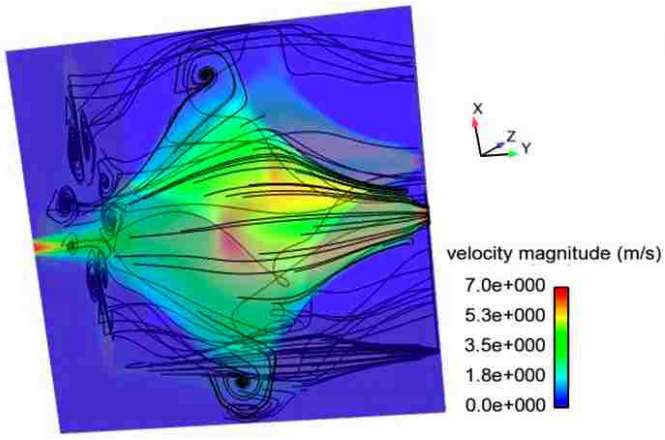

Figure 5.16: Flow streamlines through domain at 10% roughness height at $Re = 83$.

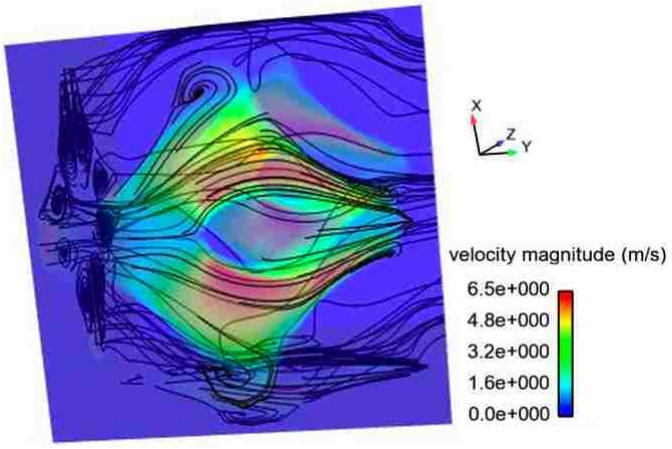

Figure 5.17: Flow streamlines through domain at 20% roughness height at $Re = 79$.

Table 5.1: Flow properties of rough BCC sphere arrangement.

Roughness	ϕ	**k** (D)	$\tau \approx \tau_1$	$\beta \times 10^3$ (m^{-1})
0%	0.3206	11.70	1.227	75.5
5%	0.3203 (↓ 0.09%)	11.52(↓ 1.48%)	1.237(↑ 0.77%)	94.9(↑ 25.72%)
10%	0.3184 (↓ 0.68%)	10.73(↓ 8.22%)	1.286(↑ 4.73%)	163.2(↑ 116.26%)
15%	0.3132 (↓ 2.32%)	9.64(↓ 17.60%)	1.365(↑ 11.28%)	319.1(↑ 322.75%)
20%	0.3039 (↓ 5.21%)	8.53(↓ 27.05%)	1.443(↑ 17.56%)	370.0(↑ 390.21%)

The tortuosity, permeability and beta factor calculated from our LBM simulation results for the rough domains with the corresponding percentage increase (↑) or decrease (↓) in the values, as the case may be, when compared to those of the smooth BCC sphere arrangement are summarized and presented in Table 5.1.

5.3.1 Disordered Sphere Pack

Having validated the method on the computer generated periodic BCC sphere arrangement, flow was simulated in the irregularly arranged sphere pack using the density gradient approach for pressure gradient with no flow boundaries on the sides of the sample and $\lambda = 0.9$. The results for tortuosity and permeability are presented in Table **??**. The difference in values of the directional estimates of the tortuosity and permeability confirms that the domain is not isotropic, although the permeability values compare well with the Carman-Kozeny estimate obtained using the domain porosity. In addition, the tortuosity is greater than that for regular BCC arrangement since the spherical particles are irregularly distributed. As a result, fluid particles flowing through the two samples travel through a larger average distance in the disordered sphere pack compared to that in BCC smooth sphere arrangement. Furthermore, the directional tortuosities and permeabilities are inversely proportional since directions with longer flow paths offer more resistance to flow, and hence will have lower permeability compared to those of directions with smaller tortuosity. However, beta factor was not calculated because inertia dominated flows could not be simulated for the given resolution as the maximum Reynold's number obtained before non convergence of flow due

Table 5.2: Flow properties of disordered sphere pack domain

Direction	**k** (md)	τ	τ_1
x	16.40	1.575	1.578
y	16.57	1.573	1.576
z	15.02	1.682	1.670
$k_{Kozeny} = 16.41$ D		$\phi = 0.407$	

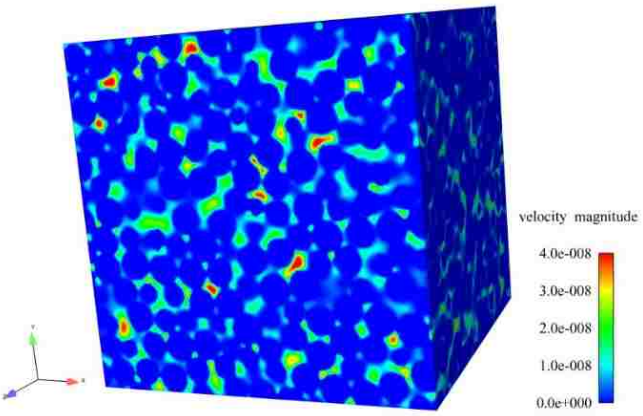

Figure 5.18: Flow distribution in 3D domain of random distribution of spheres at $Re \approx 0$.

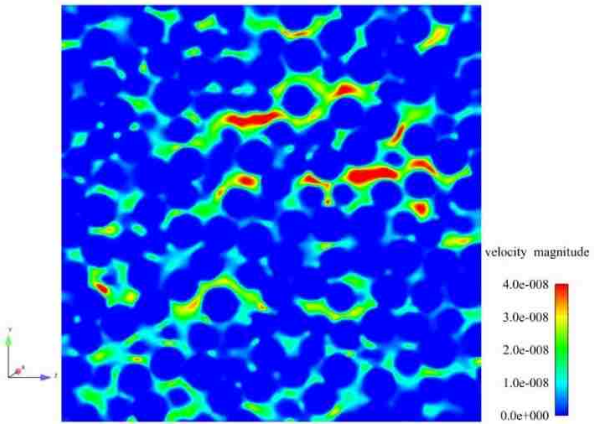

Figure 5.19: 2D slice of velocity distribution in random sphere pack at $Re \approx 0$.

to compressibility errors was low. For this computational domain, $D_p \approx 21\ lu$ and applying Equation 5.1, $Re_{max} \approx 9.0$.

The velocity distribution obtained from the LBM simulations are shown in Figs. 5.18 and 5.19. Even though inertia dominated flow could not be simulated globally in the domain, inertial contributions can be identified locally in regions with small pore sizes and hence, high velocities as represented by the hot colors in the figures above.

5.4 Realistic Porous Media

5.4.1 Permeability, Tortuosity and Beta factor of Castlegate Sandstone

The porosity of the castlegate sample was reported to be 19%, the original segmented image had a porosity of 18.50% while the value for the subset ($300 \times 300 \times 300$ voxels) chosen for

simulation was 18.2%. The closeness of the porosity value of the subset used for simulation indicates that it is representative of the original image from which it was taken. Flow is simulated in the **x, y** and **z-** directions respectively of the sample and the flow parameters are obtained from the simulation results. For this sample, the body force approach is used to implement the pressure gradient as compressibility effects becomes very pronounced (and mass is not conservation globally) for low porosity systems at high pressure gradients when density gradient approach is used. Directional permeability components are calculated from the LBM simulation results at steady state, at low values of average velocity using Equation 4.9, where Equation 4.4 is used for the body force pressure gradient.

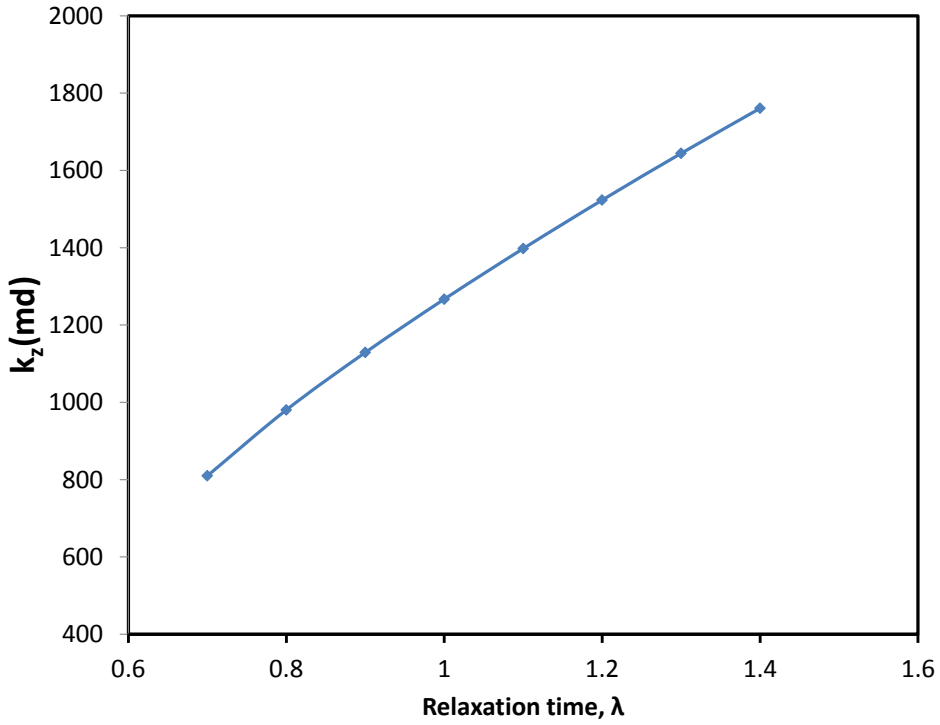

Figure 5.20: Variation of Castlegate sandstone permeability with relaxation time.

The choice of the relaxation time is made by simulating apparent permeability under low pressure gradients for different relaxation times as presented in Fig. 5.20. Unlike the BCC sphere pack in which simulation results were almost independent of the relaxation time,

Table 5.3: LBM determined flow properties of Castlegate sandstone imaged at 7.57 μm resolution

Direction	τ	τ_1	**k** (md)	$\beta \times 10^7$ (m^{-1})
x	2.577	2.738	1092	10.00
y	2.606	2.801	1036	7.299
z	2.465	2.593	1129	3.552
$k_{experiment} = 1040$ md			$\phi = 0.1802$	
$\beta_{experiment} = 4.53 \times 10^6 - 8.17 \times 10^7$ m^{-1}				

for the Castlegate sandstone, a larger decrease in permeability with reduction in relaxation time is observed. This is because for systems with complex pore-solid boundaries like the Castlegate sandstone sample, the change in the location of the bounceback node between a pore and a solid node is more pronounced than for regular systems like the BCC sphere pack and hence, greater effect of relaxation time on simulated permeability. A relaxation time of 0.9 as recommended in literature (He et al. 1997), (Zou and He 1997) is used for further analysis and the tortuosity and apparent permeability obtained at different flow velocities are plotted against the pseudo-Reynold's number and shown in Figs. 5.21, 5.22 and 5.23 respectively. From Fig. 5.23, apparent permeability is constant at low flow conditions and then decreased at higher values of the pseudo Reynold's number as inertia dominate the flow. A similar transition trend is also observed for the tortuosities, however for all directions, τ_1 estimates increase beyond the transition region while τ decreased beyond the region. This is explained by the fact that Equation 4.8 for τ_1 captures the effect of flow recirculation at high flow rates by dividing the sum of the velocity magnitudes by the sum of the directional velocity component, while Equation 4.4.3 for τ does not reflect the recirculation, since it divides the magnitude sums by the sum of the moduli of the particular velocity component. The intrinsic tortuosities and directional permeability estimates from the LBM simulations are presented in Table 5.3.

Non-Darcy coefficients in **x, y** and **z-**directions respectively are obtained by plotting the inverse of the apparent permeabilities against the pseudo-Reynolds number as shown in Figs.

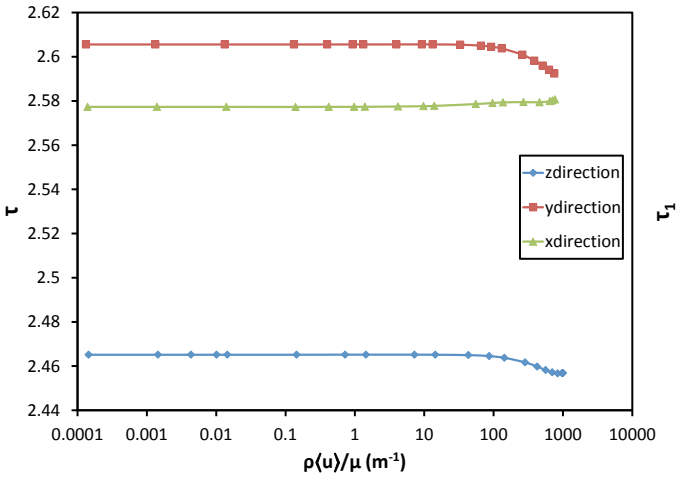

Figure 5.21: Castlegate tortuosity (τ).

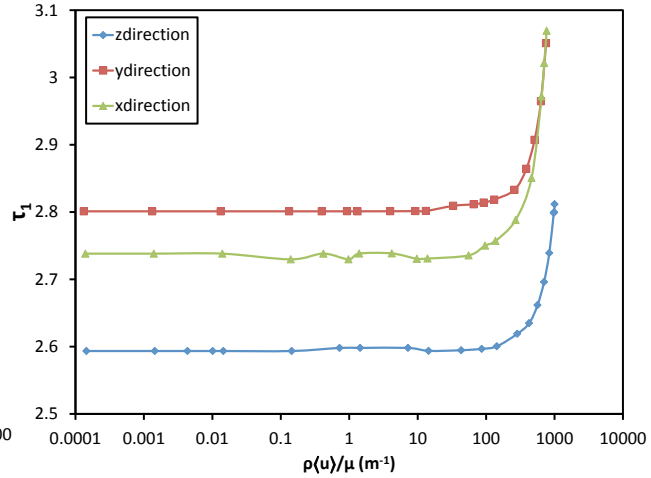

Figure 5.22: Castlegate tortuosity (τ_1).

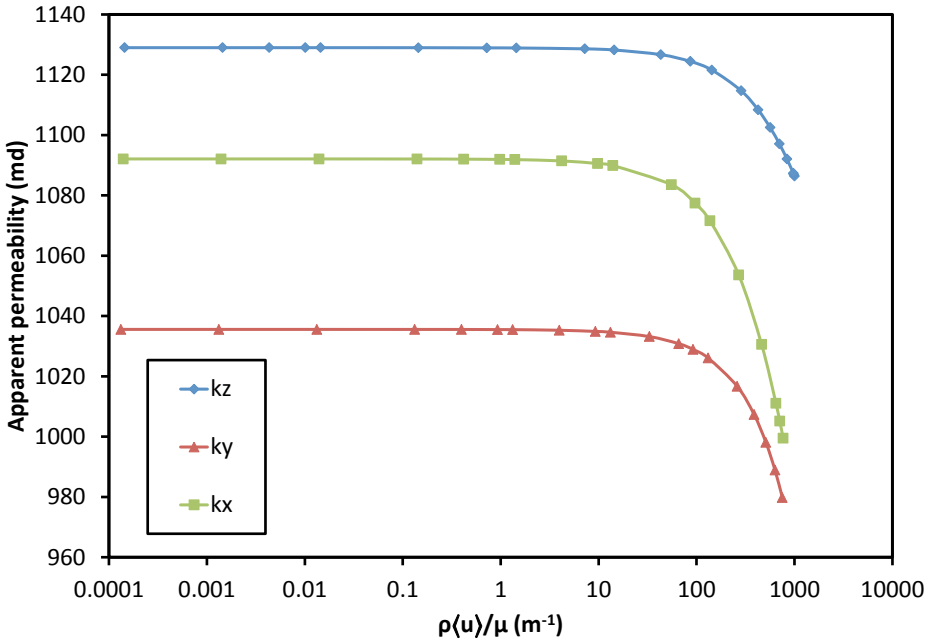

Figure 5.23: Castlegate sandstone permeability at different flow regimes (pseudo-Reynolds number).

5.24. Straight line graphs are obtained with intercepts approximately equal to the intrinsic directional permeabilities and from which directional beta factors are calculated as slopes of the graphs and also presented in Table 5.3.

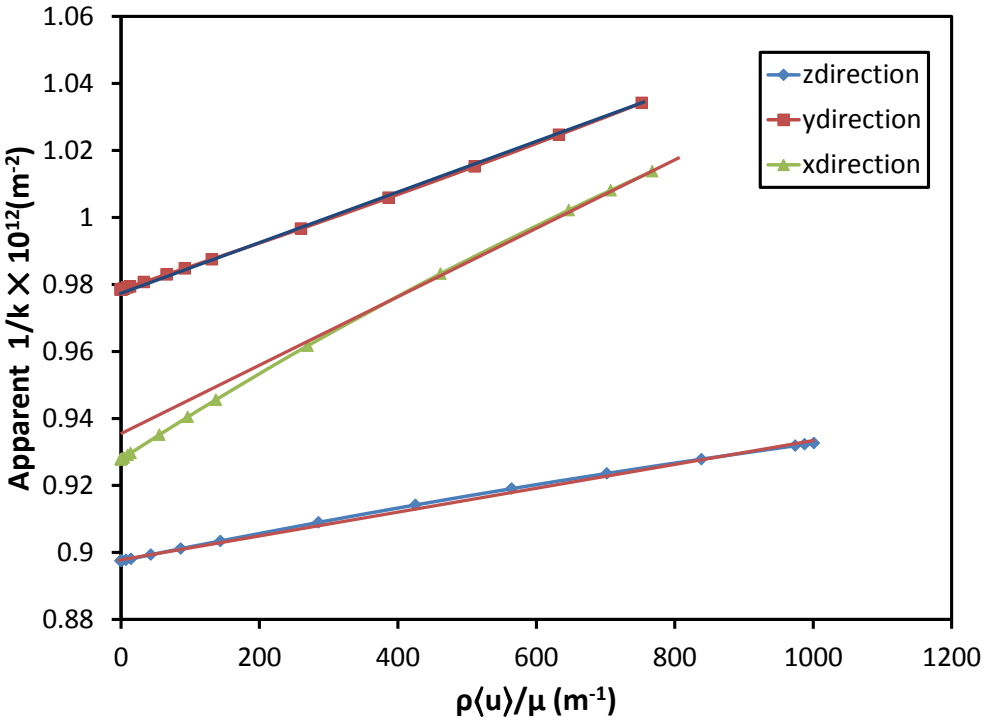

Figure 5.24: Inverse of LBM simulated apparent permeability versus pseudo-Reynolds number for Castlegate sandstone at $7.57\mu m$ resolution.

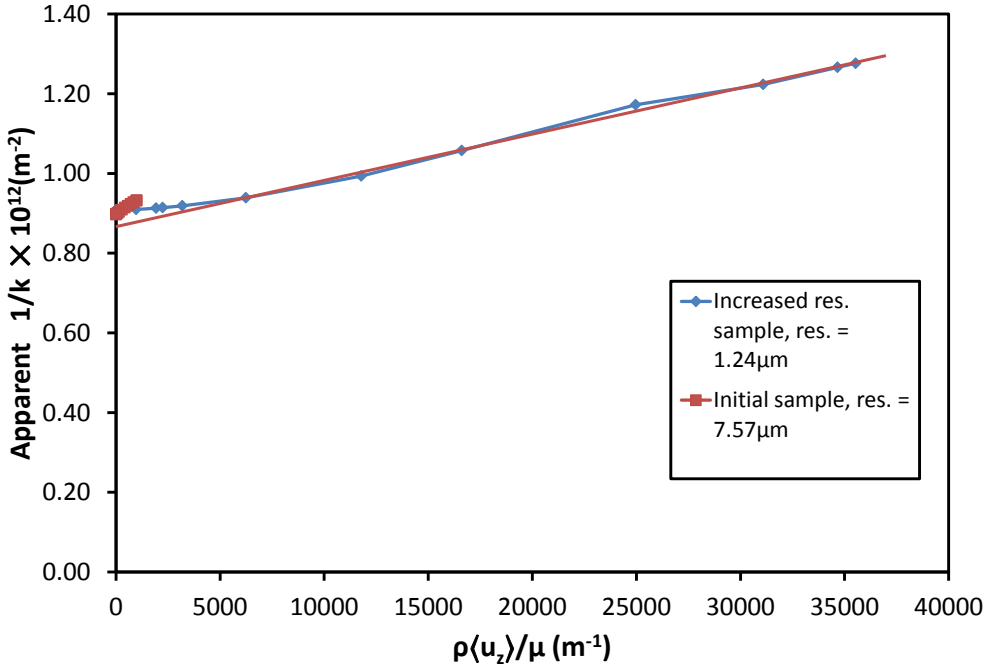

Figure 5.25: Inverse of k_z versus pseudo Reynolds number for Castlegate sandstone.

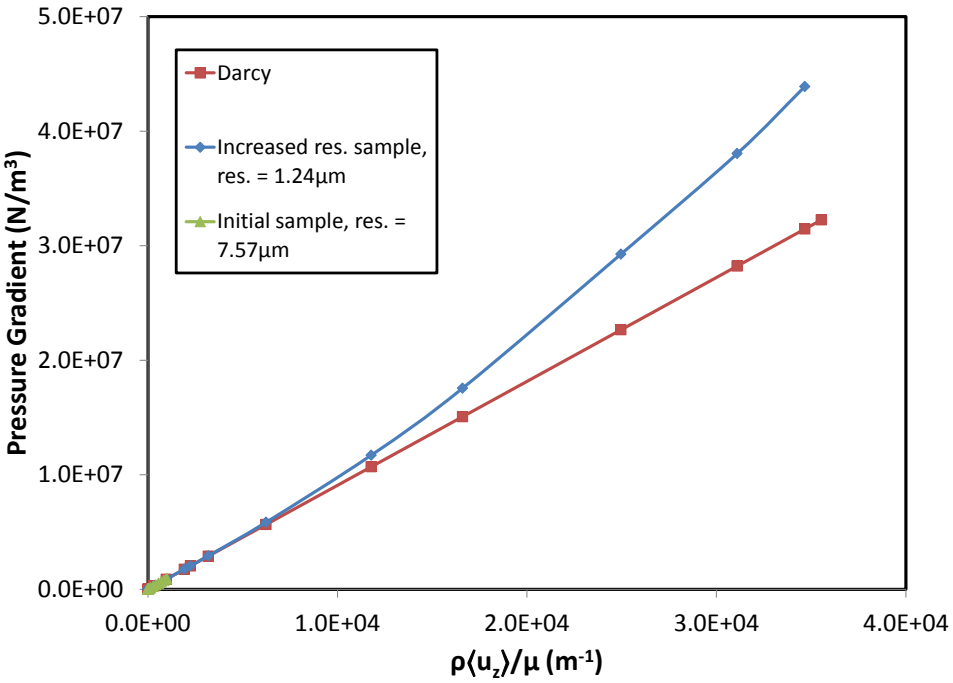

Figure 5.26: Simulated pressure gradient, for different Castlegate sandstone resolutions.

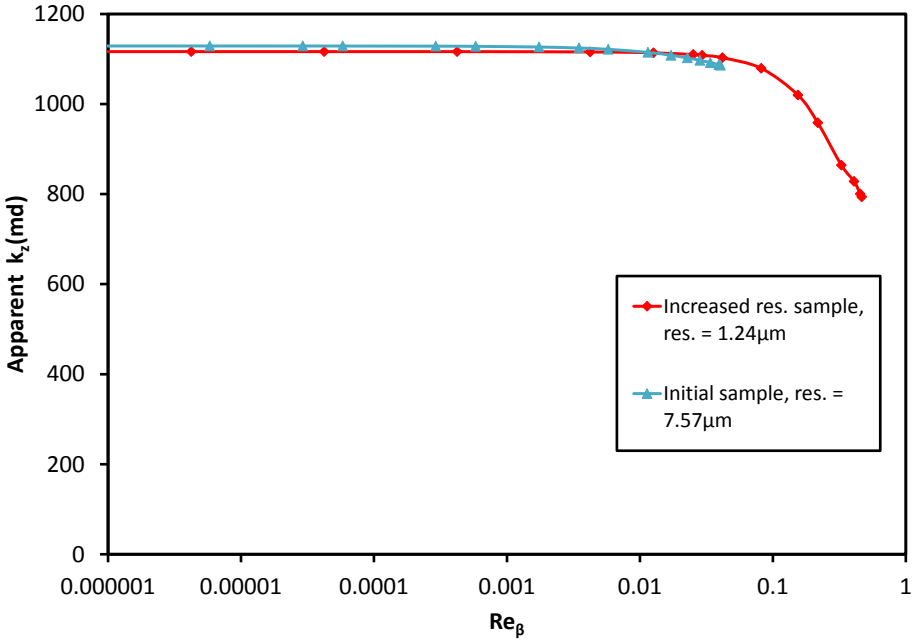

Figure 5.27: Apparent permeability versus Forchheimer number for Castlegate sandstone.

Table 5.3 also contains the experimental values of permeability and beta factor for the Castlegate sandstone. LBM permeability estimates are in agreement with the experimental value

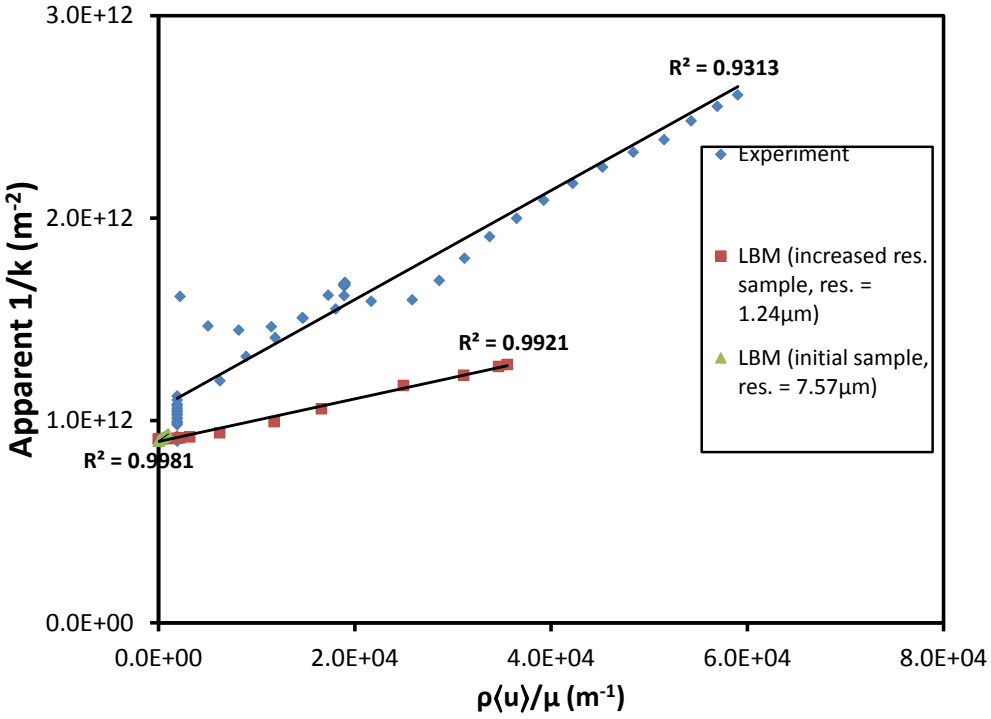

Figure 5.28: Experimental (White 2010) and LBM simulation results.

while Forchheimer coefficient from LBM simulation in the three directions are within the reported experimental range. Also, the larger values in tortuosity estimates compared to those of the BCC and disordered sphere packs show that the fluid particles move through highly tortuous pathways as they flow along different directions from inlet to outlet.

Having obtained permeability and tortuosity of the sample using LBM simulation results, we compare our beta factor estimates with a number of empirical formulations for beta factor calculation (Li and Engler 2001). These relations, listed in Table 5.4, depend on permeability, tortuosity and/or porosity. The second column of the table gives the model equations, the third column outlines the required unit of the input permeability and the unit of the output beta factor. Permeability used in these relations are the directional estimates obtained from LBM simulation results, sample porosity is $\phi = 0.182$ while τ_1 is used as the sample tortuosity for models that require tortuosity. As seen in the fourth column of the table, a wide range of

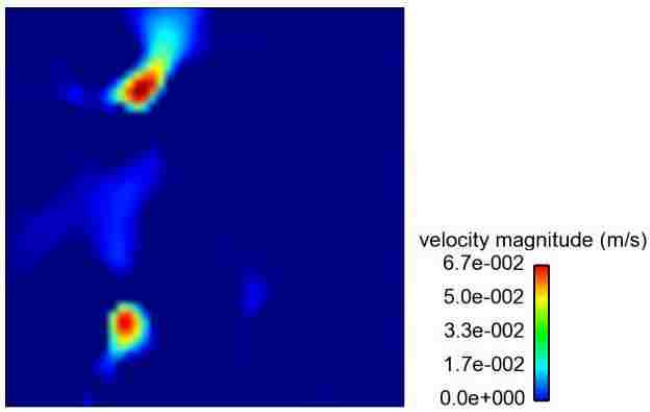

Figure 5.29: Velocity distribution on **x** mid-plane of 7.57 μm resolution ($1-50, 1-50, 1-50$ voxels subset) Castlegate sandstone at $\nabla p \approx 9.08 \times 10^5$ N/m^3 in **z**-direction. Flow is from bottom to top.

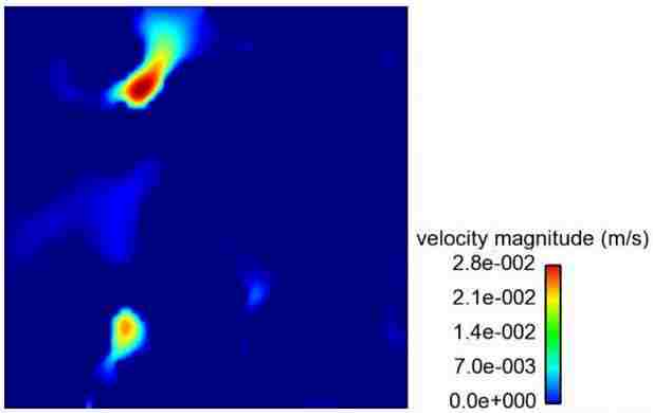

Figure 5.30: Velocity distribution on **x** mid-plane of 1.24 μm resolution ($300 \times 300 \times 300$ voxels subset) Castlegate sandstone at $\nabla p \approx 9.08 \times 10^5$ N/m^3 in **z**-direction. Flow is from bottom to top.

Table 5.4: Model results for Castlegate beta factor.

Model	**Equation**	**Model β and k units**	$\beta_x, \beta_y, \beta_z \times 10^7$ (m^{-1})
Thauvin & Mohanty	$1.55 \times 10^{12} \times \phi^{0.449} k^{-1.88}$	cm^{-1}, md	$6.806, 7.737, 5.492$
Janicek & Katz	$1.82 \times 10^{8} k^{-1.25} \phi^{-0.75}$	cm^{-1}, md	$1.04, 1.112, 0.998$
Geertsma	$0.005 k^{-0.5} \phi^{-5.5}$	cm^{-1}, cm^2	$5.650, 5.802, 5.557$
Pascal et al	$4.8 \times 10^{12} k^{-1.176}$	m^{-1}, md	$128.3, 136.6, 123.4$
Jones	$6.15 \times 10^{12} k^{-1.55}$	ft^{-1}, md	$0.3941, 0.4279, 0.3743$
Liu et al	$8.91 \times 10^{8} k^{-1} \phi^{-1} \tau$	ft^{-1}, md	$4.027, 4.344, 3.689$
Coles & Hartman	$1.07 \times 10^{12} k^{-1.88} \phi^{0.449}$	ft^{-1}, md	$0.3171, 0.3505, 0.2979$
Cooper et al	$10^{-3.25} k^{-1.023} \tau^{1.943}$	cm^{-1}, cm^2	$5.633, 6.216, 4.899$

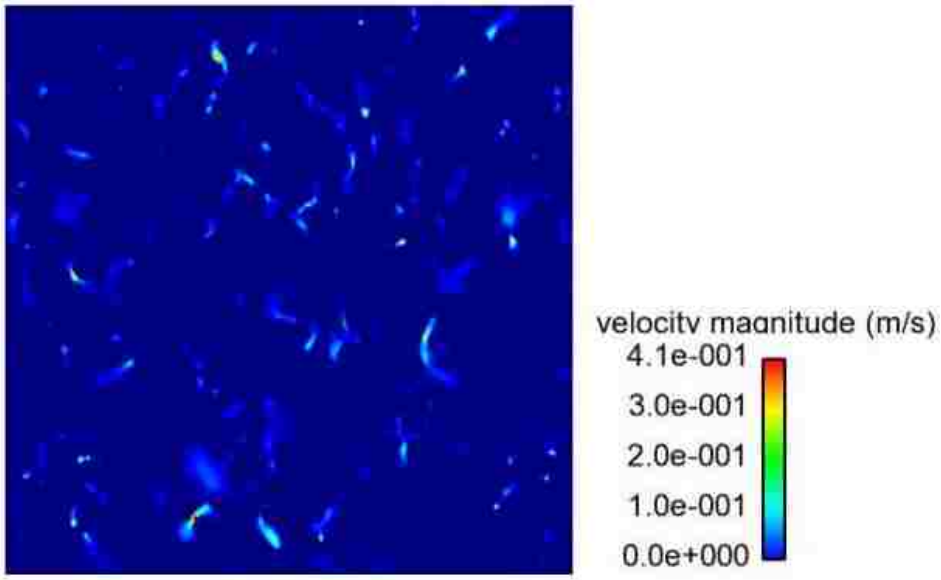

Figure 5.31: Velocity distribution on **x** mid-plane of $1-300, 1-300, 1-300$ voxels subset of 7.57 μm resolution Castlegate sandstone at $\nabla p \approx 9.08 \times 10^5$ N/m^3 in **z**-direction. Flow is from bottom to top.

beta factors ranging from about $10^6 - 10^9$ m^{-1} were obtained using the empirical relations. Although most correlations predict a non-Darcy coefficient of the order of $10^6 - 10^7$ m^{-1}, the Pascal correlation estimates $\beta \approx 1.28 \times 10^9$ m^{-1}, which is over two orders of magnitude greater than the result of the other models. This difference in the prediction of beta factor by the correlations outlines the difficulty in using empirical formulas to model flow parameters since different models give different estimates of the parameter. Comparing results of the fourth column of Table 5.4 with LBM obtained beta factors presented in Table 5.3, there is good comparison between both sets of data since most data in Table 5.4 are of the same order of magnitude as the LBM simulation result.

5.4.2 Effect of Resolution on Castlegate Simulation Result

As earlier mentioned, resolution of the computational domain has a major effect on LBM simulation results, like in other computational fluid dynamics methods. In Sec. 5.2.1, the contribution of resolution on flow permeability was quantified for the BCC smooth sphere arrangement and its effect on the simulation result was not significant since BCC domain

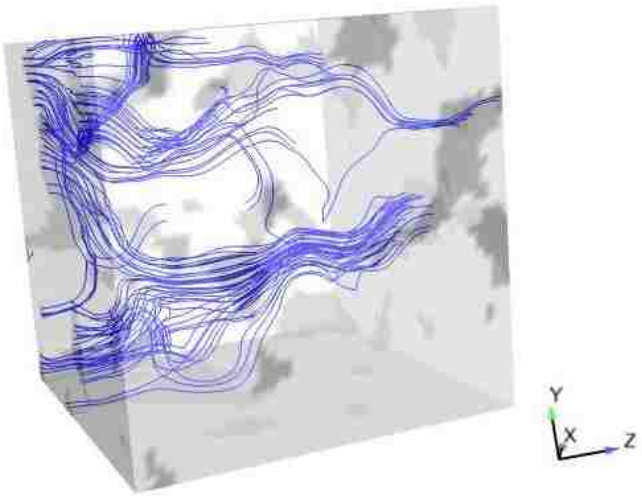

Figure 5.32: Flow streamlines through 7.57 μm resolution ($50 \times 50 \times 50$ voxels subset) Castlegate sandstone at $\nabla p \approx 9.08 \times 10^5$ N/m^3 in **z**-direction

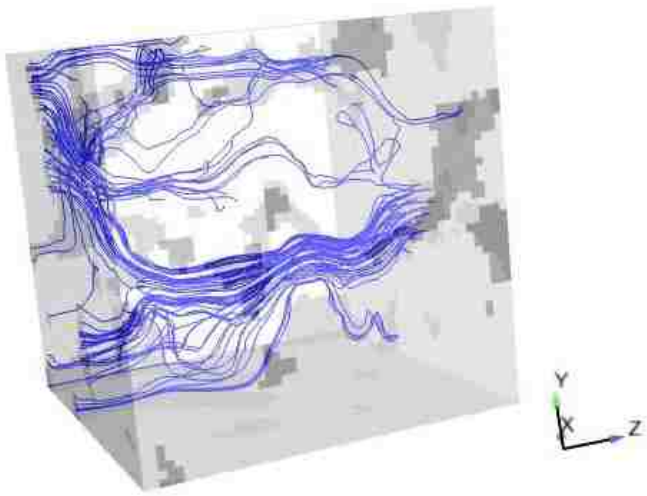

Figure 5.33: Flow streamlines through increased resolution ($300 \times 300 \times 300$ at 1.24 μm.) Castlegate sandstone at $\nabla p \approx 9.08 \times 10^5$ N/m^3 in **z**-direction.

geometry is regular with high porosity while the different resolutions (computational sizes) studied were adequate to resolve the pore spaces. However, resolution becomes very important for samples with low porosities, tight pore spaces and complex boundaries, typical of the Castlegate sandstone, especially for simulating flows in the high Reynolds number regimes. Quantifying the effect of resolution is particularly important for this Castlegate sample since it was reported that some pore spaces were resolved with as low as one voxel (personal communication with Dr. K. Thompson). This can be shown to be highly inadequate by applying Equation 5.1 but with D_{plu} representing the characteristic diameter of the pore spaces. Thus, it is obvious that high Re flows can only be simulated with very high sample resolutions which guarantees large characteristic pore diameter of the sample.

The tomography image of the Castlegate sandstone was supplied at a fixed resolution of 7.57 μm and a sample size of $300 \times 300 \times 425$ voxels. Resolution of this original sample is increased by infilling each voxel with thirty six smaller voxels (six in each direction) of the same indicator function to obtain a new sample of size $1800 \times 1800 \times 2550$ voxels at a

Table 5.5: Flow properties of Castlegate at 1.24 μm resolution

ϕ	τ	τ_1	k_z (md)	$\beta_z \times 10^7$ (m^{-1})
0.1786	1.861	1.878	1116	1.190

resolution of 1.24 μm. This way, the geometry and porosity of the original sample is preserved while providing more pore spaces on which to simulate fluid flow. Mathematically, the increase in resolution increases $\frac{\Delta x}{\Delta t}$ in Equation 3.16, resulting in increased physical value of the fluid velocity. Due to limitation of computing resources, the first $300 \times 300 \times 300$ voxels subset of the new sample was used for simulation. Its porosity is $\phi = 0.1786$. This subset is the same as the first $50 \times 50 \times 50$ voxels of the original sample but with resolution (domain size) increased by a factor of about six.

Fluid flow in the **z-**direction is simulated on the new subset with increased resolution to obtain the results in Table 5.5. The permeability of this sub-domain compares well with that of the original sample while the tortuosity and beta factor estimates are smaller than those of the previous sample. The differences in the flow parameter estimates for the two samples is due to the fact that the samples are slightly different as reflected in the difference in the their porosities.

Detailed analysis of the effect of resolution is made by comparing the simulation results for the two different sample subsets with resolutions of 7.57 μm and 1.24 μm respectively as shown in Figs. 5.25, 5.26 and 5.27. From Fig. 5.25 which shows the inverse of the **z-**direction apparent permeability at different pseudo-Reynolds number values, simulation results for the sample at 1.24 μm extends to higher pseudo-Reynolds values of up to 40000 m^{-1} compared to those of the sample at 7.57 μm with maximum pseudo-Reynolds of about 3000 m^{-1}. Fig. 5.26 shows the applied pressure gradient curves versus pseudo-Reynolds for the two samples, both in Darcy (linear) and non-Darcy (nonlinear) regimes, on the same plot. Again, the high

resolution sample permits simulation of larger pressure gradient values before the upper limit of lattice velocity is reached, compared to the low resolution sample. As a result of the low simulated pseudo-Reynolds regimes for the low resolution sample, the deviation of the total pressure gradient curve from the Darcy flow curve is not obvious. However, deviation of total pressure drop from linear Darcy pressure gradient is obvious for the high resolution sample.

To quantify the onset of flow deviation from Darcys law for the Castlegate sample, we plot a graph of permeability versus Reynolds number. However, in this case, unlike in the distribution of spheres and other regular obstructions for which the equivalent particle diameter is known, we follow the concept used by several authors including Geerstma (1974), Jones (1987), Zeng and Grigg (2006) and Green and Duwez (1951) for real porous media in which the characteristic length is defined in terms of the permeability and beta factor. According to Zeng and Grigg (2006), two types of Reynolds number criteria are used for non-Darcy flow in porous media. They are; Type-I represented by Equation 2.1 applied mainly for columns of packed particles in which the characteristics length, usually representative particle diameter, is available, and Type-II, represented by Equation 5.3, also known as the Forchheimer number, used mainly in numerical modeling of complex porous media.

$$\mathrm{Re}_\beta \text{ (and Fo)} = \frac{k\beta\rho u}{\mu} \tag{5.3}$$

Using the **z**-direction permeability and beta factor for the two samples reported in Tables 5.3 and 5.5 to calculate the Forchheimer number, a plot of the apparent permeability versus Forchheimer number is made and shown in Fig. 5.27. Deviation from the constant apparent permeability regime occurs at $Re_\beta \approx 0.02 - 0.08$ for the two samples which is consistent with the value of $Re_\beta = 0.005 - 0.2$ reported by both Ruth and Ma (1993) and Zeng and Grigg (2006).

Furthermore, experimental result by White (2010) is converted to a format comparable with the LBM simulation results by calculating the apparent permeability at different flow conditions (pseudo-Reynolds) followed by plotting and fitting the data with a straight line, on the same graph as the **z**-direction LBM flow results for the two sample subsets. Fig. 5.28 shows this plot. Although the slopes (beta factor) of the experimental and 1.24 μm resolution sample data are different as seen from the graph, their values are of the same order of magnitudes viz., $3 \times 10^7 \mathrm{m}^{-1}$ and $1 \times 10^7 \mathrm{m}^{-1}$ respectively. Interestingly, it is observed that although data for the 7.57 μm sample occupies just a small region with a slope of about $4 \times 10^7 \mathrm{m}^{-1}$, its results will closely match the experimental data if flow is simulated up to the same flow regimes as the experimental results, since they have similar slopes.

Finally, we capture the effect of resolution on flow distribution by showing velocity and streamlines through the sample at different resolutions, as shown in Figs. 5.29, 5.30, 5.31, 5.32 and 5.33. Figs. 5.29 shows velocity distribution through a 2D slice of the 7.57 μm, $1 - 50 \times 1 - 50 \times 1 - 50$ voxels subset while Fig. 5.30 is the velocity distribution through the same sample subset but at the increased resolution (1.24 μm). It is seen that velocity distribution in the increased resolution samples are better resolved compared to the distribution in the original sample subset. This difference in the velocity resolution is responsible for the variations and extent of flow results obtained from the LBM simulation. In addition, Fig. 5.31 shows velocity distribution on a 2D slice of the 7.57 μm resolution sample, but of $1 - 300 \times 1 - 300 \times 1 - 300$ voxels size. It shows a collection of pore spaces with poorly resolved velocity distributions in them.

As earlier mentioned, increasing the sample resolution creates more connected pore spaces which become available for fluid flow. This is observed by comparing Figs. 5.32 and 5.33 which show flow streamlines through the $1 - 50 \times 1 - 50 \times 1 - 50$ voxels subset, at the

original and increased resolutions respectively. Streamlines in Fig. 5.33 are more disordered compared to those of Fig. 5.32 and this is because the additional pore voxels opens up poorly resolved pore spaces and channels in the original sample that otherwise were not in the connected flow path. This is seen in new pore channels at the bottom of the outlet face in Fig. 5.33 which are not observed in Fig. 5.32.

Chapter 6
Conclusion

6.1 Conclusion

In this work, the benefits of using lattice Boltzmann method to simulate fluid flow in systems characterized by complex boundaries, like porous media, are outlined. Using both body force and density gradient approaches with the bounce back scheme to implement the no-slip boundary condition between the solid and the fluid phases, the method is validated on 3−dimensional domains of regular and irregular distribution of spheres. Thereafter, flow was simulated on a real porous media, the Castlegate sandstone with complex geometries like uneven pore-grain boundaries and low porosity composed of intra- and inter-particle pore spaces. From the volume averaged simulation results, the media permeability, tortuosity and beta factor are estimated and compared with the Ergun and Kozeny equation estimates for the validation cases and experimental results for the Castlegate sandstone.

Validation results show good comparison for permeability and non-Darcy coefficient between LBM simulation and the Kozeny and Ergun estimates respectively. Also, from the plot of apparent permeability against Reynolds number, two regimes are observed; the viscous dominated regime characterized by constant permeability and the inertia regime characterized by decreasing permeability at increasing Reynold's number. The transition from the viscous dominated Darcy regime to the inertia dominated non-Darcy regime is well within the range ($Re \approx 1 - 10$) reported in literature for regular sphere packs. Also, the effects of roughness on the media flow parameters are quantified by simulating flow in the same geometry as one of the validation cases, but with roughness defined as hemispherical protrusions on the particles. Presence of roughness increased the flow path length and thus, increased the tortuosity and non-Darcy coefficients while decreasing the permeability since the domain became

more resistant to flow as compared to the smooth arrangement. In addition, the Castlegate sandstone permeability of $1092 - 1116$ md and beta factor estimates of $1 \times 10^7 - 10 \times 10^8 \mathrm{m}^{-1}$ obtained from LBM simulation results are in good agreement with experiment values of 1040 md and $4.53 \times 10^6 - 8.17 \times 10^7 \mathrm{m}^{-1}$ respectively while empirical predictions of the beta factor using LBM calculated permeability and tortuosities showed wide variation in values in the range of $4 \times 10^6 - 1.37 \times 10^9 \mathrm{m}^{-1}$, although the estimates of most of the correlations analyzed are of the same order of magnitude as the simulation result. Using the LBM beta factor estimate and Type-II Reynolds number defined by Zeng and Grigg (2006), the calculated transition range obtained in this work is within the values given by Ruth and Ma (1993) and Zeng and Grigg (2006).

The LBM algorithm was implemented using the open source codes, OpenLB and Palabos which were run on high performance computing resources and we reached regimes in which over a billion grid variables of computations were carried out at the rate of millions of lattice site update per second. In addition, the codes scaled well on the multiple processors and showed increasing computational speed as more nodes were used.

6.1.1 Recommendation

From the findings of this work , several aspects of our simulation results and the LB method deserve further studies. These includes:-

Models less Dependent on Relaxation Time

The LBM results are much dependent on the relaxation time for the BGK model. Even the MRT model for complicated pore/solid boundaries, like the Castlegate sandstone sample, still show some dependence on relaxation, though less so compared to the BGK model. To improve the reliability of the LBM results, it is imperative to use models whose results are

less dependent on the relaxation time. This is important especially when the LBM is to be applied to systems in which effects like rarefaction and compressibility are encountered.

Compressibility Effect

Compressibility effects are a major issue for low porosity systems when pressure gradient to drive flow is implemented by density difference. LBM guarantees accurate results only at slightly compressible regimes. For low porosity samples, high pressure gradients (high flow rate conditions) can only be implemented by large density gradients which invariably introduce fluid compressibility in an incompressible fluid system. The effect is that mass is not conserved globally.

Mach Number Limit

$Ma = 0.1$ places a limit on the range of lattice flow velocity and hence the upper limit on the Reynolds number that can be simulated. This means that for systems with small length dimensions, only by increasing the resolution can high flow rate conditions be simulated. Models that relax the Mach number limit while still not compromising the result accuracy should be used.

6.1.2 High Sample Resolution

Samples of porous media to be used for LBM flow simulations should be at high resolutions to guarantee high Reynolds number regimes.

Bibliography

Barree, R.D., and M. W. Conway. 2004. "Beyond Beta Factors: A Complete Model for Darcy, Forchheimer, and Trans-Forchheimer Flow in Porous Media." *SPE*, no. 89325.

Cancelliere, A., C. Chang, E. Foti, D. Rothman, and S. Succi. 1990. "The permeability of a random medium:comparison of simulation with theory." *GEOPHYSICS* 2:2085–2088.

Chen, S., D. Martinez, and R. Mei. 1996. "On boundary conditions in lattice Boltzmann methods." *Physics of Fluids* 8 (9): 2527–2236.

Coles, M. E., and K. J. Hartman. 1998. "Non-Darcy Measurements in Dry Core and the Effect of Immobile Liquid." *SPE*, no. 39977.

D'Humieres, D., I. Ginzburg, M. Krafczyk, P. Lallemand, and S. Luo, L. 2002. "Multiple-relaxation-time lattice Boltzmann models in three dimensions." *Phil. Trans. R. Soc. Lond.* 360:437–451.

Ergun, S. 1952. "Fluid flow through packed columns." *Chem. Eng. Prog.* 48:89–94.

Feichtinger, C. 2005. "Drag Force Simulations of Particle Agglomerates with the Lattice-Boltzmann Method." Master's thesis, INSTITUT F INSTITUT FUR INFORMATIK.

Ferreol, B., and D. H. Rothman. 1995. "Lattice-Boltzmann simulations of flow through Fontainebleau porous media." *Transport in Porous media* 20:3–20.

Forchheimer, P. 1914. "Leipzig and Berlin, Teuner." *Hydolik*, pp. 116–118.

Geerstma, J. 1974. "Estimating the coefficient of inertial resistance in fluid flow through porous media." *SPE Journal*, pp. 445–450.

Green, L., and P. Duwez. 1951. "Fluid flow through porous medium." *Journal of Applied Mechanics*, pp. 39–45.

Guo, Z., and C. Zheng. 2002. "An extrapolation method for boundary conditions in lattice Boltzmann method." *Physics of Fluids* 14:2007–2010.

Habich, Johannes. 2006. "Improving computational efficiency of lattice Boltzmann methods on complex geometries." Master's thesis, INSTITUT F INSTITUT FUR INFORMATIK.

Hassanizadeh, S. M, and W. G. Gray. 1987. "High velocity flow in porous media." *Transport in Porous Media* 6 (2): 521–531.

He, X., Q. Zou, L.S. Luo, and M. Dembo. 1997. "Analytical Solutions to Simple Flows and Analysis of Nonslip Boundary Conditions for the Lattice Boltamann BGK Model." *Journal of Statistical Physics* 87:115–136.

Hernandez, H. J. L. 2004. "Optimal Fracture Treatment Design for Dry Gas Wells Maximizes Well Performance in the presence of Non-Darcy Effects." Master's thesis, Department of Petroleum Engineering, Texas A&M University.

Holditch, S. A., and R. A. Morse. 1976. "The effects of non-Darcy flow on the behavior of hydraulically fractured gas wells." *Journal of Petroleum Technology*, pp. 1169–1179.

Huang, H., and J. Ayoub. 2006. "Applicability of the Forchheimer Equation for Non-Darcy Flow in Porous Media." *SPE*, no. 102715.

Jin, G., T. W. Patzek, and D. B. Silin. 2004. "Direct prediction of the absolute permeability of unconsolidated and consolidated reservoir rock." *SPE*, no. 90084.

Jones, S.C. 1987. "Using the inertial coefficient, , to characterize heterogeneity in reservoir rock." *SPE*, no. 16949.

Latt, Jonas. 2008. *OpenLB User Guide*. 0.4. jonas@lbmethod.org: www.lbmethod.org.

———. 2011. www.lbmethod.org/forum/read.php?3,792,2947msg-2947. www.lbmethod.org/forum/read.php?3,792,2947msg-2947.

Li, Dacun, and Thomas W. Engler. 2001. "Literature Review on Correlations of the Non-Darcy Coefficient." *SPE*, no. 70015 (May).

Lin, C., and M. H. Cohen. 1982. "Quantitative Methods for Microgeometric Modeling." *Journal of Applied Physics*, pp. 4152–4165.

LONI. 2011. www.loni.org. www.loni.org.

Mei, R., W. Shyy, D. Yu, and L.S. Luo. 2000. "Lattice Boltzmann Method for 3-D Flows with Curved Boundary." *Journal of Computation Physics* 161:680–699.

Nabovati, A., and C. M. Sousa. 2007. "Fluid flow simulation in Random porous Media at Pore Level using the lattice Boltzmann Method." *Journal of Engineering Science and Technology* 2 (3): 226–237.

Okabe, H. 2004. "Pore-Scale Modeling of carbonates." Ph.D. diss., University of London and Imperial College London.

Oren, P. E., and S. Bakke. 2003. "Reconstruction of Berea sandstone and pore-scale Reconstruction of Berea sandstone and pore-scale Reconstruction of Berea sandstone and pore-scale modelling of wettability effects." *Journal of Petroleum Science and Technology* 39:177–199.

Rigby, S.P., and L.F Gladden. 1996. "NMR and Fractal Modelling Studies of Transport in Porous Media." *Chemical Engineering Science* 51 (10): 2263–2272.

Rothman, D. 1988. "Cellular-automaton fluids: A model for flow in porous media." *GEOPHYSICS* 53 (4): 509–518.

Rushing, J. A., K. E. Newsham, P. M. Lasswell, J. C. Cox, and T. A. Blassingame. 2004. "Klinkenberg-Corrected Permeability Measurements in Tight Gas Sans: Steady-State versus Unsteady State Techniques." *SPE*, no. 89867.

Ruth, D., and H. Ma. 1992. "On the derivation of the forchheimer equation by means of the averaging theorem." *Transport in Porous Media* 793:225–264.

———. 1993. "The Microscopic Analysis of High Forchheimer number Flow in Porous Media." *Transport in Porous Media* 13:139–160.

Struchtrup, Henning. 2005. *Macroscopic Transport Equations for Rarefied Gas flows*. 1860-6245. Springer.

Succi, S, E. Foti, and F. Higuera. 1989. "Three-dimensional flow in complex geometries with the lattice Boltzmann method." *Euro Physics Letters* 10:433–438.

Thauvin, F., and K. K. Mohanty. 1998. "Network Modeling of Non-Darcy Flow Through Porous Media." *Transport in Porous Media* 31, no. 19.

Timm Kruger, Fathollah Varnik, Dierk Raabe. 2009. "Shear stress in lattice Boltzmann simulations." *Physical Review* 79, no. 046704 (April).

Torskaya, T., G. Jin, and C. T. Verdin. 2007. "Pore-level analysis of the relationship between porosity, irreducible water saturation, and permeability of clastic rocks." *SPE*, no. 109878.

Whitaker, S. 1996. "The Forchheimer Equation: A Theoretical Development." *Transport in Porous Media* 25:27–61.

———. 1999. *The Method of Volume Averaging.* Volume 13. P.O.box 17, 3300 AA Dordrecht, The Netherlands: Kluwer Academic Publishers.

White, Chris. 2010, June. "Preliminary analysis of high flow rate data on castlegate Sandstone, EM09-3C-1." Technical Report, LSU.

Zeng, Z., and R. Grigg. 2006. "A criterion for non-Darcy flow in porous media." *Transport in Porous Media* 63:57–69.

Zou, Qisu, and Xiaoyi He. 1997. "On pressure and velocity flow boundary conditions and bounceback for the lattice Boltzmann BGK model." *Physics of Fluids* 9 (6): 1591–1598 (June).

Appendix: Nomenclature

Symbols	Description	SI Units
K	Permeability tensor	m^2
∇p	Pressure gradient	N/m^3
μ	Dynamic viscosity	Ns/m^2
$\langle \vec{u} \rangle$	Volume averaged velocity vector	m/s
q	Flow rate	m^3
A	Cross sectional area	m^2
$\tau \& \tau_1$	Tortuosity	No unit
D_p	Particle diameter	m
a_v	Specific surface area	m^{-1}
β	Beta factor	m^{-1}
ρ	Fluid density	kg/m^3
ϕ	Porosity	No unit
$f_\alpha(\vec{x}, \vec{e}_\alpha \partial t)$	Particle distribution function	No unit
$\vec{e}_\alpha$	Phase velocity vector	No unit
Ω	Collision operator	No unit
ν_{lu}	Lattice kinematic viscosity	No unit
λ	Dimensionless relaxation time	No unit
S	Collision matrix	No unit
M	MRT transformation matrix	No unit
$\hat{S}$	Diagonal collision matrix	No unit
c_s	Lattice speed of sound ($c_s^2 = \frac{1}{3}$)	Lattice units

Vita

Chukwudi Chukwudozie was born on 1^{st} of November, 1983, in Abuja, Nigeria, to Patrick and Comfort Chukwudozie. He attended Federal Government College Abuja for secondary school education and graduated in 1999. He then proceeded to the Federal University of Technology Minna, Nigeria, from where he earned a Bachelor of Engineering in Chemical Engineering in 2006. Thereafter, he proceeded to Louisiana State University, Louisiana, U.S.A., for graduate studies and is currently a candidate for the Master of Science in Petroleum Engineering, to be awarded in May 2011.

Chukwudi is an avid lover of soccer. He also plays golf, tennis, ping-pong and enjoys swimming.